INTERIM PERFORMANCE REPORT

NASA Grant Number: NASA/JWST grant NAG5-12460

ASU Grant Number: AWA 6068

Project Start: Sept. 2002
Project End: Aug. 2021
Reporting period: Jul. 2012–Oct. 2013
Submission Date: Nov. 22, 2013

Title: Interdisciplinary Scientist for the James Webb Space Telescope

Proposal Title: Next Generation Frontier Studies of Galaxy Formation and Evolution with NGST: Building on and Learning from the HST Heritage, and Pushing the New Frontiers.

PI: Rogier A. Windhorst, Regents' and Foundation Professor

Email: Rogier.Windhorst@asu.edu

Institution: Arizona State University

Investigators: (for this last year):

Rogier A. Windhorst (Regents' and Foundation Professor, ASU)
School of Earth & Space Exploration
550 E. Tyler Mall, Room GWC-508
Arizona State University
P.O. Box 871404
Tempe, AZ 85287-1404, USA
Tel: +1-480-965-7143 or 9416 or 8950
FAX: +1-480-965-6362
Email: Rogier.Windhorst@asu.edu

Dr. Seth H. Cohen (Research Scientist, ASU, Tempe, AZ)

Dr. Rolf A. Jansen (Senior Research Scientist, ASU, Tempe, AZ)

Other collaborators not paid for by NASA/JWST

Abstract: In this report, we summarize the results of three projects ongoing at ASU in support of the JWST science mission. These are, together with their main results thus far:

I: How Can Straylight and Possible Gradients be Removed from JWST Deep Survey Images?

We use the HST/WFC3 XDF data to simulate a range of rogue-path or straylight amplitudes ($\lesssim$35–95% of Zodi) and gradients ($\lesssim$2–5% as fraction of the total background; Bowers 2013) that could affect ultradeep JWST images. We justify and present an iterative, image-transposing, 1D fitting algorithm that removes this superimposed signal successfully from the simulated JWST images. The algorithm can recover the affected images to the point that the straylight signal and gradients or higher-order spatial variations therein are essentially removed. We show that the straylight+gradient subtracted ultradeep images allow Source Extractor to recover the catalog completeness that was present before such signal was imposed, except of course for the noise penalty resulting from the additional straylight signal. This appears to be true even in the worst case of a "pedestal" of $\sim$95% of Zodi with $\sim$4% spatial variations, ranging in shape from a linear slope to a 2×2-component higher-order surface.

II. Predicting JWST Number Counts for z$\gtrsim$10 using the HUDF WFC3 IR data

Only one possible candidate has been detected at z$\simeq$10–12 in the 522 hr HST/WFC3 XDF. This number is affected by image crowding and cosmic variance. We suggest that this low number may imply a significant drop in the Schechter M^* (or Φ^*) values with redshift at z$\gtrsim$8, consistent with predictions from some recent hierarchical models.

If so, *deep to ultradeep* JWST NIRCam surveys (*i.e.*, 25–150 hours per filter) respectively) may be required to reach fainter than M^* at z$\gtrsim$10 and detect a significant number of objects at z$\gtrsim$10 to AB$\lesssim$31–32 mag. For a possible parameter landscape of M^* (z)–Φ^* (z)–α(z) — based on our current knowledge — we suggest that the number of objects detected at z$\simeq$10–12 may range from 15–50 objects to AB$\lesssim$31 mag (4×25 hr) to 60–180 objects to AB$\lesssim$32 mag (4×150 hr) per JWST/NIRCam pointing. The uncertainty on these numbers is at least 0.3–0.5 dex due to image crowding, cosmic variance, and the current poor statistics at high redshifts.

Medium-Deep JWST surveys (AB$\lesssim$30 mag) may detect far fewer objects at z$\gtrsim$10, since they may not reach fainter than M^* at those redshifts, unless they target deliberately chosen, well-studied foreground lenses.

III. Using Group Lensing to Optimize JWST First Light Surveys

The consequence of II could be that shallower JWST images ($\lesssim$few hours) that reach to AB$\lesssim$30 mag may have to be pointed at foreground lensing clusters or rich compact groups, in order to find a significant number of First Light objects at redshifts z$\simeq$10–20.

We outline a strategy to identify and prepare an optimal sample of massive groups and clusters at z$\gtrsim$0.3–0.4, that may be used across the sky as gravitational lenses to optimize the number of "first light" objects detected in medium-deep (AB$\lesssim$30 mag) JWST surveys. These are selected from the GAMA survey, which we discuss in detail.

Topics II and III will be the subject of our main IDS research at ASU in the next several years to assure an optimal implementation of our proposed IDS GTO Medium-Deep JWST survey.

1 I. How Can Straylight and Possible Gradients be Removed from JWST Deep Survey Images?

Authors: Rogier A. Windhorst, Seth H. Cohen, & Rolf A. Jansen

1.1 Introduction: Possible Out-of-field Straylight plus Possible Gradients in Deep JWST Images

The JWST sunshield and optics design/fabrication may add some out-of-field 1–5μm straylight mainly from the Galactic plane and Galactic Center to the in-field Zodiacal foreground in (ultra)deep JWST images (Bowers et al. 2013).

This straylight comes from truant light-paths in the JWST spacecraft, and therefore may not carry the full PSF of the JWST Optical Telescope Element (OTE). The major components come from near scatter off the primary mirror, scatter off the frill surrounding the primary mirror, the secondary mirror support structures (struts), and the truant light-paths (Bowers et al. 2013). The direct (specular) rogue path component has been blocked. The remaining rogue path component would be near-specular scatter off the pick-off mirror, and should generally be a relatively small contributor. Altogether, the straylight can amount to $\sim$30–50% (*i.e.*, $\sim$0.28-0.44 mag) in amplitude to the in-field Zodiacal background, or higher in some specific fields (Bowers et al. 2013). Since the Zodiacal background of JWST in L2 over ground-based is $\sim 10^3$–$10^4\times$ darker in H-band–4μm, respectively, the corresponding $\sqrt{(1.3-1.5)}$ decrease in sensitivity due to any of the additional rogue-path light is not likely a significant limitation to the ultimate 1–5μm JWST image depth, and is in any case it is within the JWST straylight requirements.

Since Galactic near–mid-IR sources show (strongly) varying structure on (sub-)arcmin scales, the JWST straylight can possibly have (sub-)arcmin gradients with amplitudes typically $\lesssim$2–5% of the total background (ı.e. $\sim$25.2–26.2 mag arcsec^{-2} ; Bowers et al. 2013). These numbers are likely upper limits, since more recent ray-tracing studies by NASA GSFC and contractors suggest that they may be lower. In random deep JWST fields, such gradients can be removed, as we will outline below. If needed, careful planning/scheduling using optimal dithering/drizzling, the acquisition of sky-flats, and/or observing the field under different roll angles may help to accurately measure and subtract the effects from large-scale low-level sky-gradients from each location.

Significant gradients in this rogue-path light could make the detection and construction of very faint object samples more difficult in (ultra)deep JWST fields, *if* the majority of the pixels are covered by objects including their outer wings. Similarly, straylight gradients could be harder to measure and remove in JWST fields that have a very rich and complex foreground structure, such as clusters of galaxies in the HST Frontier Fields, since the straylight gradients would need to be separated from the significant intra-cluster light, which does carry the full PSF of the JWST OTE.

1.2 Simulations of Deep (JWST) Images with Rogue-Path Amplitudes and Straylight Gradients

We model the sky background through simulated JWST images generated by one of us (SHC) using the Hubble eXtreme Deep Field (ACS+WFC3) images (Bouwens, Illingworth et al. 2012; Ellis et al.2012). We will consider four cases of possible sky-backgrounds, which are summarized in Fig. 1a–1f:

(1) Only zodi background, so the sky-fit should not contain significant power in any higher order terms; or

(2) The zodi background from (1), plus an additional background due to straylight originating from Zodi and the Milky Way, modeled as a *linear gradient on a "pedestal" level*, so the fit should not contain significant power in any higher order terms; or

(3) The zodi background from (1), plus an additional background due to straylight originating from Zodi and Milky Way, modeled as a *simple 1-component lower-order 2D pattern*, which may be represented by, e.g., a spline or some other low-order, smooth function; or

(4) The zodi background from (1), plus additional background due to straylight originating from zodi and Milky Way, modeled as a *more complex (2×2 component) 2D pattern*, which may be a spline or some other higher-order, smooth function.

All four straylight surfaces were added to the 92-orbit (236.1 ksec) XDF H-band (F160W) drizzled image that reaches to AB $\lesssim$ 30 mag, which is equivalent in depth to a 2-3 hr JWST exposure (NIRCam filter F150W). This was done for three possible straylight amplitude (SA) cases, ranging from 35–95% of Zodi as summarized in Bowers et al. (2013) and in Table 1 here. To limit the computing time required, we used the 60 m.a.s. pixel version of the XDF, which is similar to the JWST NIRCam Long Wavelength Channel (LWC) pixels, although the drizzled LWC pixels will be $\lesssim$ 30 m.a.s. (and smaller still for the drizzled pixels of the Short Wavelength Channel or SWC). The smaller JWST PSF compared to HST will also help greatly, although most faint galaxies will be (just) resolved to AB $\lesssim$ 31 mag (Windhorst et al. 2008), and therefore have wings that contribute to the sky-brightness in (ultra)deep JWST images.

These adopted straylight gradients (Bowers 2013; Table 1), range in amplitude from –5% to +3% of the total background (or from –11% to +9% of the straylight amplitude itself). We assumed that the straylight gradients varied by these numbers *corner-to-corner* in the simulated XDF images. The resulting images are shown in Fig. 1a–2d, together with the entire 522 hour XDF images in the BViIzYJWH filters. The color images of Fig. 1a–1e are properly weighted averages over these 9 HUDF filters, using sky-sigma values measured in relatively object-free areas, and using a very hard log-log stretch to illustrate very faint low-SB features and the significant image crowding expected in deep JWST images.

For simplicity, the straylight amplitudes and gradients were added to the XDF H-band images only, to visually show their effects and how they are best removed. In reality, the source of the JWST rogue-path light (our Galaxy and the Galactic center in particular) is rather red. In future, straylight pedestals plus gradients can be added to all JWST NIRCam filters like "riJH" (+"KLMN", which would have to be simulated from scratch, since WFC3 only reaches to 1.73μm), with colors representing the old Galactic stellar population that may cause the rogue path light. For the purpose of showing how large these straylight gradients could be, their effect on catalog completeness, and how well they can be corrected for, it is sufficient to only simulate the H-band filter here.

A more recent study by Bowers et al. (Sept 2013) reports 2μm straylight of similar amplitudes, but of significantly lower straylight gradients than adopted in Table 1. This is the consequence of the design and implementation of the new frill of the JWST Optical Telescope Element (OTE). This is good news for JWST, because it means that while the overall amplitudes of the JWST straylight may be similar to the ones simulated below, their gradients may be substantially smaller. Hence,

Table 1. Summary of StrayLight Amplitudes and Gradients Added to the XDF H-band

Gradient Case	Zodi(H) (AB arcsec^{-2})	2μm Zodi (MJy/sr)	Straylight Ampl. MJy/sr (% Zodi)	Straylight Gradient MJy/sr (% of Total)
Rms HUDF	22.70	0.095	0.033 (35%)	0.0066 (–2.3% to +2.8%)
Worst Case	22.75	0.091	0.086 (95%)	0.0138 (–5% to +3%)

the straylight gradient cases simulated here — and how well they can be removed — serve as an *upper limit* to the actual case currently expected for JWST. It is possible that the 1–5μm straylight gradients are low enough that only JWST programs with exposure times $>>$1 hr per pointing (*i.e.*, JWST deep fields) may need to be corrected for straylight gradients. If low-level sky-background gradients are in fact seen shallow JWST images, then our software package presented below can remove them, or a user can plan to construct sky-flats from properly dithered images to add in their removal. As we will see, our simulated worst-case straylight gradients can still be removed with the code that we developed for this purpose, even in the very crowded XDF and JWST images. The only permanent noise-penalty, of course, is essentially that of the flat straylight amplitude or pedestal that was added to the images.

1.3 Fitting the Sky-Background in Crowded Deep-Field Images with Straylight Gradients

The 522 hour HST WFC3 XDF has $\sim$45% of its drizzled pixels covered by faint galaxies, including their detectable outskirts (Koekemoer et al. 2013). That is, determining any remaining low-level sky-gradients from the image itself becomes a daunting task, that has not been pursued to these SB-levels before. It is *a priori* not clear, therefore, that this straylight gradient removal is a solvable problem. Hence, we must make sure that we understand the straylight amplitude, its gradients and their implications for JWST's ultradeep images.

When a CCD (or IR detector) image is not very deep (AB$\lesssim$26 mag), most pixels contain empty sky that is not noticeably contaminated by the detected outskirts of faint galaxies to within the sky+read-noise present (e.g., Neuschaefer & Windhorst 1995). However, when CCD or IR images reach to very faint SB-levels, such as the XDF to AB$\lesssim$30 mag (point source sensitivity), the outskirts of (faint) galaxies start to partially overlap to the point that far less empty sky is available for a robust assessment and subtraction of the sky-background (e.g., Windhorst et al.2008). As a consequence of significant image crowding, object finding algorithms (such as Source Extractor; Bertin & Arnouts 1996) may therefore start missing a fraction of faint objects. This is referred to as the "natural confusion limit", where very deep image catalogs may become gradually incomplete, not due to the lack of instrumental resolution, but because of the blocking of background objects by (the wings of) brighter foreground galaxies, and because the outskirts of foreground galaxies also start to statistically overlap with each other (Windhorst et al. 2008).

Hence, when ultradeep CCD or IR images have a significant fraction of the pixels covered by real objects and their wings, low-level large-scale gradients will be harder to remove. In the case of shallow images — where most of the pixels just cover empty sky — low-level large-scale gradients

can be removed by 2D spline fitting to a grid of boxes that are filled with iteratively (one-sided) 2σ-clipped median or modal sky-values (Neuschaefer & Windhorst 1995). For this to work, the modes need to be determined from largely empty sky-boxes that are large enough to properly exclude most real objects in the σ-clipping, and small enough to properly sample the spatial frequencies present in the remaining sky-gradient. If needed, the resulting grid of modal sky-values can be further (one-sided) 2σ-clipped to weed out the minority of boxes whose sky-modes are still significantly affected by brighter objects.

In the case of the XDF with $\sim$45% sky-coverage by objects to AB$\lesssim$30 mag (Koekemoer et al. 2013), our experience is that 2D spline fits can no longer be used to measure and remove low-level large-scale sky-gradients. Every box in the grid is simply filled with objects to the point that a well-clipped, reliable median or sky-mode can no longer be determined iteratively. Each drizzled 2k$\times$2k or 4k$\times$4k image would not allow for a sufficiently large number of *uncorrupted* sky-boxes to survive the 2σ-clipping process, leaving too many holes in the grid for the 2D spline to be reliably fit to. Stated differently, by using clipped median or mode boxes, the very large number (4M–16M) of image pixels is reduced to relatively few ($\lesssim 10^3$) sky-box modal values, far too few of which accurately represent the sky-background and its low-level gradients for a fully 2D spline-fit to work reliably. Moreover, a fully 2D spline fit has cross-terms that tend to amplify brighter objects that remain in affected sky-boxes. We therefore had to abandon the idea to fit a fully 2D spline-surface to the remaining XDF of JWST sky to reliably determine and subtract any low-level large-scale background gradients.

1.4 Method: 1D-Fitting of the Sky in Deep Fields through Iteratively-Transposed Images

Our main back-ground removal routine will instead do an iterative *1D-fit* of the sky-background along rows (X) and columns (Y) *separately* up to a user-specified order in X and Y (default order=5). Rows and columns are thus fitted *each separately in 1D*, again using aggressive one-sided $\lesssim 2\sigma$-clipping as appropriate for the XDF or deep JWST images.

To speed up the process numerically on the expected drizzled 4k$\times$4k–8k$\times$8k JWST images, the 1D-fit is first done along the X-axis on all rows, then the image is transposed, and the same process is repeated along the Y-axis *which is now temporarily also sorted along rows*. The image transposition is thus purely done to speed up the CPU usage of the algorithm. Once the Y-axis fits are done, the image is then transposed back, and the whole process is iterated until it converges. The process is first done in 0th order (*i.e.*, determine the best clipped sky-value as a 0th order constant along each row and transposed column), then in 1st order (*i.e.*, determine the best clipped linear sky-fit along each row and in each transposed column), then in 2nd order, etc, until the maximum order (default 5) is reached in both X and Y.

For this process to work, the image has to be rectangular without partially unexposed outskirts, so it can be usefully transposed and fit properly in successive iterations. I.e., the common cross section of the (larger) FITS image with the fully exposed sky-area has to be determined first, and the fully exposed area must be excised before the 1D (X, Y)-fitting routine is applied. The weight maps resulting from image drizzling are not used in the fitting process or to identify the full area to be used, but if needed this can be implemented later. Some borders of fully exposed pixels are left outside the fitted area on each side to help stabilize the higher-order fits inside that area (see Fig. 1e).

The algorithm thus deliberately does not have cross-terms for the following reasons: (1) a fully 2D algorithm with cross-terms (such as a 2D spline) would not properly work on the ultradeep HST and JWST images, as discussed above; (2) it would be computationally more expensive; and (3) as it turns out below, the 1D sky-fitting algorithm on the repeatedly fitted and transposed images works remarkably well, removing almost all of the visible sky-gradients without creating large artifacts, while allowing subsequent Source-Extractor runs to recover most of the faint objects and their flux.

Given the way our gradient-removal algorithm is implemented, the higher order fitting terms determined by iteratively transposing the image make up in part for the cross-terms that are absent from the fit, which would not have allowed the sky-fit to converge to a proper solution on the ultradeep and crowded images.

1.5 Implementation of the 1D Iteratively Transposing Gradient-Fitter

To implement this 1D sky-fitting process on ultradeep HST and JWST images, we wrote an IDL package similar to "autofilet.pro' (Jansen et al. 2003), that was written to remove electronic "herring-bone" patterns from STIS CCD images (Jansen et al. 2003b), preserving the the basic book-keeping and FITS I/O code of "autofilet.pro". We implemented the iterative, image-transposing 1D fitting algorithm in IDL as a new routine called "rjbgfit.pro", which has the specific task to remove a smooth low-order background with unknown order and unknown shape in a very crowded HST or JWST field.

We created a mask image using 'SAOImage ds9' to define the polygonal region of interest to be fit. We used the distortion-corrected full HUDF H-band mosaic as input, but inserted the simulated backgrounds in the *un-illuminated* as well as the *illuminated* pixels, because the drizzled HST WFC3 IR mosaics come as FITS files that are rotated with North up, so the illuminated areas will in general have some diamond shape, and the unilluminated area is also part of the FITS file.

We want to fit the background in the illuminated regions only. We already know that this background is of fairly low-order. So having a jump in signal at the boundaries of the illuminated area will cause a problem for a line-by-line fit along both rows and transposed columns. Even when masked, such a fit would be meaningless for the image borders and corners. Hence, we have to set these unilluminated pixels back to zero to properly run the gradient-removal algorithm, since there is extra information on the imposed gradients in those unilluminated pixels, that real JWST observers won't have.

To implement this aspect, we define a polygon-shaped ''ds9" *regions* file that contains all the properly illuminated pixels and no other pixels. We save the resulting regions file in "DS9 format" using "physical" coordinates. We convert this "regions" file into a mask image using a custom routine ''mkmask" (Jansen 2013), and use this mask to set the values of all masked pixels in the simulated JWST images to zero. Hence, only the illuminated area of interest remains to be fit.

We now have image frames that may be comparable to what JWST users will be confronted with. The background gradients may not have high enough S/N that they can or need to be removed from the *individual* pipeline-processed flat-fielded images, so instead we will fit the background and its gradients in the *final stack* of co-added frames that are drizzled onto some regular undistorted pixel grid.

For the purpose of 1D fitting a gradient background using iterative image transposition, we are less concerned about correlated pixel-noise and loss of resolution in faint objects. Hence, we can physically rotate and resample the image onto a more suitably oriented pixel grid in preparation for the sky background fit, and ignore the outer-most border of a few pixels width.

We need to sample pixels along virtual pixel lines/columns that are oriented at a random sky ORIENT angle with respect to the frame buffer axes. Therefore, we de-rotate the image, using an angle of 90-38.92806 = 51.07194 deg for the XDF. We also tested if the rotation algorithm conserved flux. The total flux in the rotated image is 0.0127% lower than in the original image, which may be due to round-off errors in getting the image statistics using IRAF task 'imstat'. This is quite acceptable for our purposes.

Next, we perform the 1D iteratively transposed fit. We added an explicit condition to the core IDL routine "splfit.pro" to exit *if* the normal exit condition has not been reached in 1000 iterations, which during the testing phase occasionally happened. The result obtained for each successive fit-order along a row or transposed column is added to to the sky-model for that line, in such a way that we iteratively approach our final model, while correcting for deviations and artifacts introduced in previous (lower-order) fits. This results in an image with a reasonable first-order model for the sky-background and its gradients removed, but with the sky-background and its gradients still somewhat effected by the brighter objects in the image.

Therefore, we next carry out an object detection step to produce an object mask that includes all objects in the image bright enough to affect the previously fitted low-order sky-background values. For this, we perform one-sided 2σ-clipping on all rows and transposed columns individually. Pixels with values $\gtrsim 3.0\sigma$ *also* have their *neighboring* pixels rejected at the $\gtrsim +0.5\sigma$ level to optimize rejecting the effects from galaxy wings or PSF-wings on the 1D results. Finally, we repeat the higher order row and transposed column fits only on those pixels that have been excluded by this object mask. We then add these higher order fits to the best sky-background fit, replacing the previous higher order fits that could still be significantly affected by objects that were present in the image. This results in a sky-background plus gradient image that is to a much better degree unaffected by the discrete objects present in the image, as illustrated in Fig 1a-1e and all panels of Fig. 2a–2d.

After convergence was obtained in the final image, we rotated the fitted background frame back to the original orientation. Finally, we subtracted the best-fit background from the original mosaic frames (see Fig. 1a–1f and 2a–2d).

For the record, the straylight amplitudes and gradients were removed by one of us (RAJ), who had no knowledge of the actual amplitudes and gradients, including their spatial frequency pattern imposed on the images, which was done by another person (SHC). The only information given to the gradient remover was that they were probably of low-order, but possibly of high amplitude.

1.6 Results on the XDF simulations representing Medium-Deep JWST images

Fig. 1aa shows the HUDF XDF data from 750 ACS+WFC3 orbits in the filters BViIzYJ140H (Koekemoer et al. 2013). All 9 filters were added with weights proportional to the sky σ^{-2} determined in clear, relatively object free areas. The resulting weighted filter–stack is in a sense a "bolometric" optical–near-IR image of the HUDF and reaches AB$\lesssim$31 mag. It is displayed with a double log *false-color* stretch to best illustrate the significant image crowding expected in deep

JWST images at AB$\gtrsim$30 mag. This rendering illustrates the significant image crowding at AB$\sim$30 mag, where $\sim$45% of the pixels are covered by the wings of objects (Koekemoer et al. 2013).

Fig. 1 shows the original XDF image at its original (1a) and a very hard log-log stretch (1b), respectively. Fig. 1c–1e show examples of the straylight gradients imposed on the XDF -H-band images — fully rendered in 9-band color — for the three amplitude cases and the four gradient geometries tested, as listed in Table 1 and §1.2.

Fig. 1f shows the resulting XDF image with the worst case gradient removed. The red box outlines the rectangular area which has the full exposure time available, where the full iterative 1D fit in X and transposed Y can take place. (There is a small fully-exposed border area outside this box, as explained in §1.5).

Fig. 2a–2d shows the straylight gradients imposed (all upper left panels), the actual background fits obtained (lower left panels), and the image with its best-fit gradient fit removed (upper left panels). A few of the very brightest stars and compact bright galaxies in the field (e.g., near the top and middle-right) left a few brighter lines in the background gradient which the code could not fully remove these very bright objects. As it turns out below, this has no measurable consequence in the catalog completeness of the background-corrected images (see Fig. 2a–2d).

To remove any remaining high-frequency structure, we subtracted for illustrative purposes Fig 2a (bottom left panel) from the similar panels in Fig. 2b–2e. The resulting background-model is now more smooth, as shown in the bottom right panels of Fig. 2b–2d. The background gradient model determined by "rjbgfit" is the one that was actually removed from the original images (upper left panels) to obtain the background-subtracted images (upper right panels).

Almost all astronomical details in the original hardly-stretched image of Fig. 1b are visible in Fig. 1f, although over a slightly smaller area and modulo the irrecoverable noise-penalty from the imposed straylight pedestal. No gross artifacts seem to have been introduced by the gradient-removing algorithm. Note the slight background depressions or "moats" present around the brightest galaxies in Fig. 1b. This is an artifact of the data reduction and drizzling process, and not of "rjbgfit", since they are visible in the original image as well (see the hardly-stretched Fig. 1b. The user may need to magnify the PDF on the screen and turn all ambient lights off to see this). These "moats" are however also somewhat decreased in negative amplitude by "rjbgfit" (see upper right panels of Fig. 2a–2d), so to first order "rjbgfit" will also sense, model and correct for negative gradients in the image, whether these are physically justified or not. We will attempt to improve on this latter aspect in a future version of the code, if needed.

1.7 Resulting Catalog Completeness in Gradient-Subtracted Images

To test quantitatively how well our the 1D iteratively transposed gradient-removal algorithm works, we inserted artificial point-like objects identically in each of the images *before and after* the 1D iteratively-transposed gradient-removal algorithm was applied. Specifically, in each of 40 magnitude bins we inserted 500 artificial objects ten times to improve the uncertainties, yielding in total 2×10^5 objects inserted in each image tested. The results are shown in Fig. 3a–3b, which is very similar to Fig. 8 of Windhorst et al. (2011) that tested the completeness and point-source sensitivity of the WFC3 ERS data. The photometry on all inserted objects was done with Source Extractor (Bertin & Arnouts 1996) using the MAG-APER option with a fixed aperture circular aperture diameter of $0''.5$. The 50% completeness limits are derived from the inflection point of a fit of an erfc(m) function, as indicated by the solid lines in each panel. Blue points and lines

indicate the completeness as a function of total H-band flux for the 10-σ detection limit, and red points and lines indicate the 5-σ detection limits. These completeness functions were normalized to unity vertically to uniformly correct the sample for the significant image crowding in the XDF, which is discussed in detail in a future paper.

The five cases of sky-gradients in §1.2 are shown as the five rows of panels in Fig. 3a–3b, *before* (all left panels) and *after* (all right panels) the gradient removal was done. Top panels are the original image with Zodi sky only, each 2nd panel just adds a *constant* rogue-path pedestal to the Zodi, each 3rd panel instead adds the *linear gradient*, each 4th panel the *single-component* 2D spline gradient, and each 5th panel the *2×2-component 2D spline gradient*. Our conclusions from Fig. 3a–3b are summarized and discussed in the next section.

1.8 Conclusions on Gradient-Removal from UltraDeep HST & JWST Images

The following are our conclusions from this project:

(1) Careful comparison of Fig. 3a–3b shows that all simulations are no more accurate than ∼0.01–0.02 mag in the quoted catalog completeness limits. This is due to the significant image crowding in the XDF, which prevents us from usefully adding *and* recovering $\gtrsim 10^4$ artificial point-like objects in each image, thereby limiting the statistics for the Monte Carlo completeness test. Also, the best sky-background plus gradient model obtained thus far (lower-left hand panels of Fig. 2a–2d) show some residual low-level line-artifacts, that could not be fully removed with the current implementation of the code as discussed above (lower left panels of Fig. 2), since some rows and columns simply intersect with too many high S/N objects in the ultra-crowded HST (or JWST) images.

If needed, we will improve on this aspect in a future version of the code. As shown below, these low-level residual line-patterns remaining after applying "rjbgfit.pro" do not significantly impact the resulting sample completeness. If needed, however, they can be removed to a better approximation *if for a given target* a good sky-flat could be made from a sufficiently large number of well dithered images (and if needed taken under different roll-angles). Such a sky-flat processed by "rjbgfit.pro" will resemble the lower-left panel of Fig. 2a. After applying the current version of the code, any residual low-level line-artifacts could be subtracted from those images *of the same field* that do show significant higher-order gradients (e.g., the lower-left panels of Fig. 2b–2d), resulting in more smooth models of the sky-background plus its gradients (as shown in the lower-right panels of Fig. 2b–2d, which all had the lower-left panel of Fig. 2a subtracted). If needed, we will address this refinement in mode detail in a future paper. For now, will assess the resulting sample completeness after applying "rjbgfit.pro" as is, including the residual low-level line-artifacts seen in the lower-left panels of Fig. 2a–2d. That is, the sample completeness recovered in the right panels of Fig. 3a–3b is based on the sky-background plus gradient models produced by "rjbgfit.pro", as shown in the lower-left panels of Fig. 2a–2d.

(2) In all cases, the *constant pedestal* rogue-path added (the 2nd row of panels in Fig. 3a–3b) just leads to the expected loss in sensitivity, which for the three cases in Table 1 is 0.14 mag, 0.21 mag, and 0.32 mag, respectively, and indeed close to the –2.5 log [$\sqrt{(imposed\ pedestal)}$]. *These pedestal losses are unavoidable, and will also occur for JWST in the case of significant straylight pedestals.* They are used as the benchmarks against which we measure the quality of the removal

of the more complex gradient surfaces. These fiducials are indicated by the vertical blue and red dotted lines that cut across the four lower panels in each of Fig. 3a–3b.

(3) In all gradient cases, the object finding algorithm SExtractor is quite forgiving with respect to any gradients present or remaining in the images, as can be seen by comparing the additional loss in sensitivity due to more complex gradient surfaces (3rd, 4th and 5th rows of panels in Fig. 3, respectively) *both before (left panels) and after (right panels) gradient removal*. This is because SExtractor already does it own background-surface determination and subtraction (Bertin & Arnouts 1996), which apparently works quite well for linear and *simple* higher order background gradients. This background-surface fitting may not work so well in Source Extractor for the more complex gradients, as seen by comparing the *bottom* panels of Fig. 3a–3b *before* (left) and *after* (right panels) gradient removal. The 1D iteratively transposing gradient removal algorithm appears to make a significant difference here. If the background gradients have more complex structures, we thus recommend the use of "rjbgfit".

(4) Both the cases of significant linear gradients (3rd row of panels), simple 1-point higher order surfaces (4th rows), and more complex 2×2 component surfaces (5th row) are fairly accurately removed. *In all cases, the catalog completeness of the original image is nearly completely restored, to within the 0.01–0.02 mag ability to assess catalog completeness.*

(5) The recovery of lost sensitivity due to the imposed complex 2×2 component surfaces — after their removal with "rjbgfit" — is as good as 0.1–0.2 mag, better than what SExtractor alone is able to provide *before* removal of the more complex gradients.

1.9 Future Work

(1) Once the first Hubble Frontier Field (HFF) data have been taken and completely reduced, we will apply a similar algorithm as "rjbgfit" on gradients imposed on the HFF cluster fields as well, and see how well we can remove those given the presence of the diffuse intra-cluster light (ICL). In the extreme case that too large a fraction of these images is simply covered by ICL, we will try to remove both sources of low-order light together with "unsharp masking" techniques — or with an appropriately modified version of "rjbgfit" — in orfer to better detect all lensed background objects that may be present in the images at $z\simeq2$–20.

(2) We will also experiment with and modify "rjbgfit" for the purpose of fully removing all large foreground cluster galaxies, and investigate if this improves the ability to make more complete catalogs of (lensed) background objects. This may also provide better catalogs of compact objects belonging to the cluster itself, such as globular clusters and dwarf galaxies.

(3) Our plan is to next use R- or I-band HUDF images where the PSF is about half the size. The completeness brighter than the 50% drop-off point in the blue/red curves of Fig. 3 is *not* zero-sloped, and this seems to depend on wavelength. We have modified the curve fitting to reflect this for the second part of study. Flatter slopes in the completeness curves may suggest that we should use the shorter wavelength data available to study effects from the PSF-size on our gradient-removal algorithm.

Acknowledgements: We thank Chuck Bowers for helpful discussions regarding the JWST stray-light models. This work was supported by NASA JWST Interdisciplinary Scientist grant NAG5-12460 from NASA Goddard Space Flight Center.

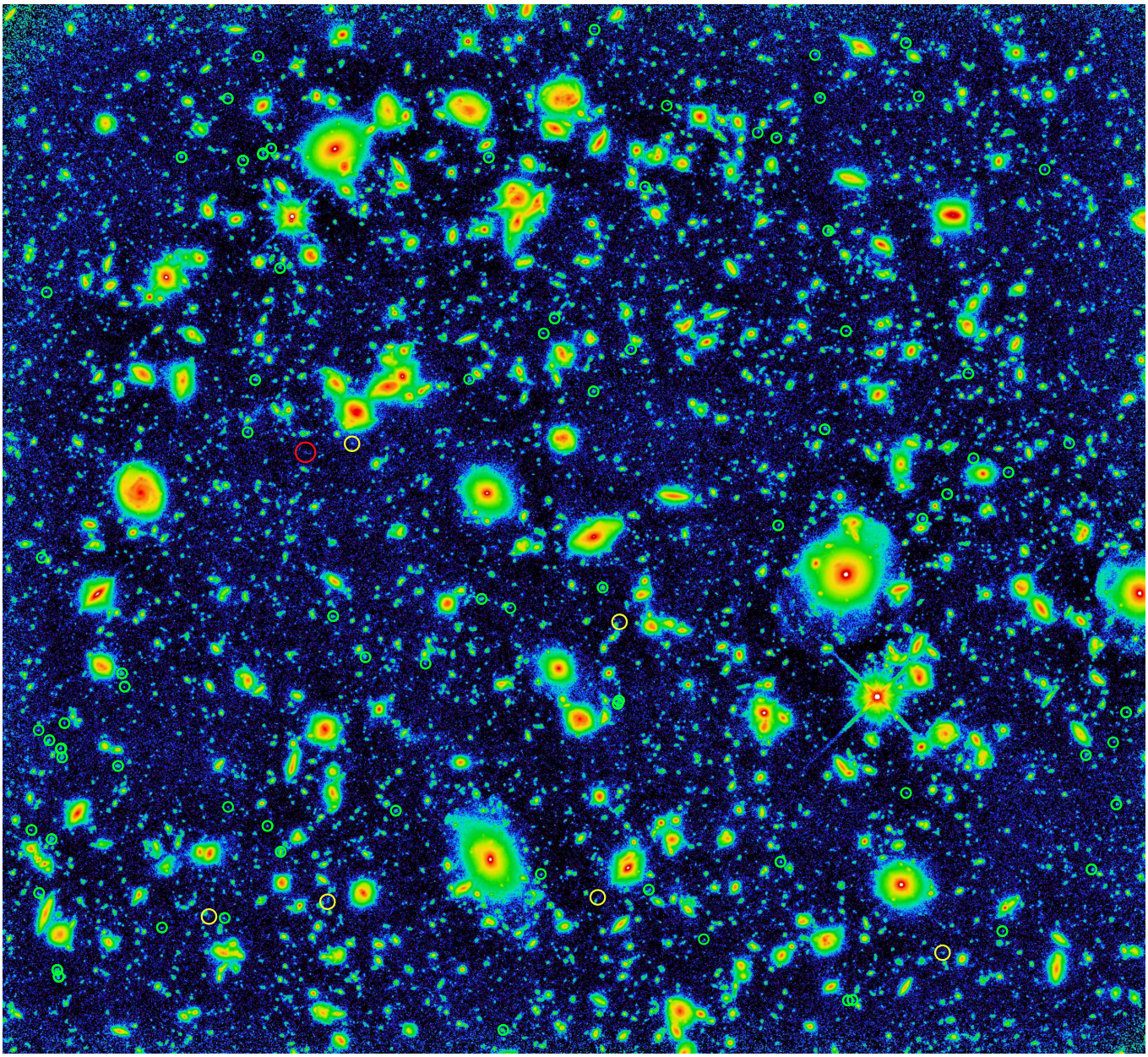

Fig. 1aa: The HUDF XDF data from 750 ACS+WFC3 orbits in the filters BViIzYJ140H (Koekemoer et al. 2013). All 9 filters were added with weights proportional to the sky σ^{-2} determined in clear, relatively object free areas. The resulting weighted filter–stack is in a sense a "bolometric" optical–near-IR image of the HUDF and reaches AB$\lesssim$31 mag. It is displayed with a double log *false-color* stretch to best illustrate the significant image crowding expected in deep JWST images at AB$\gtrsim$30 mag. This rendering illustrates the significant image crowding at AB$\sim$30 mag, where $\sim$45% of the pixels are covered by the wings of objects (Koekemoer et al. 2013).

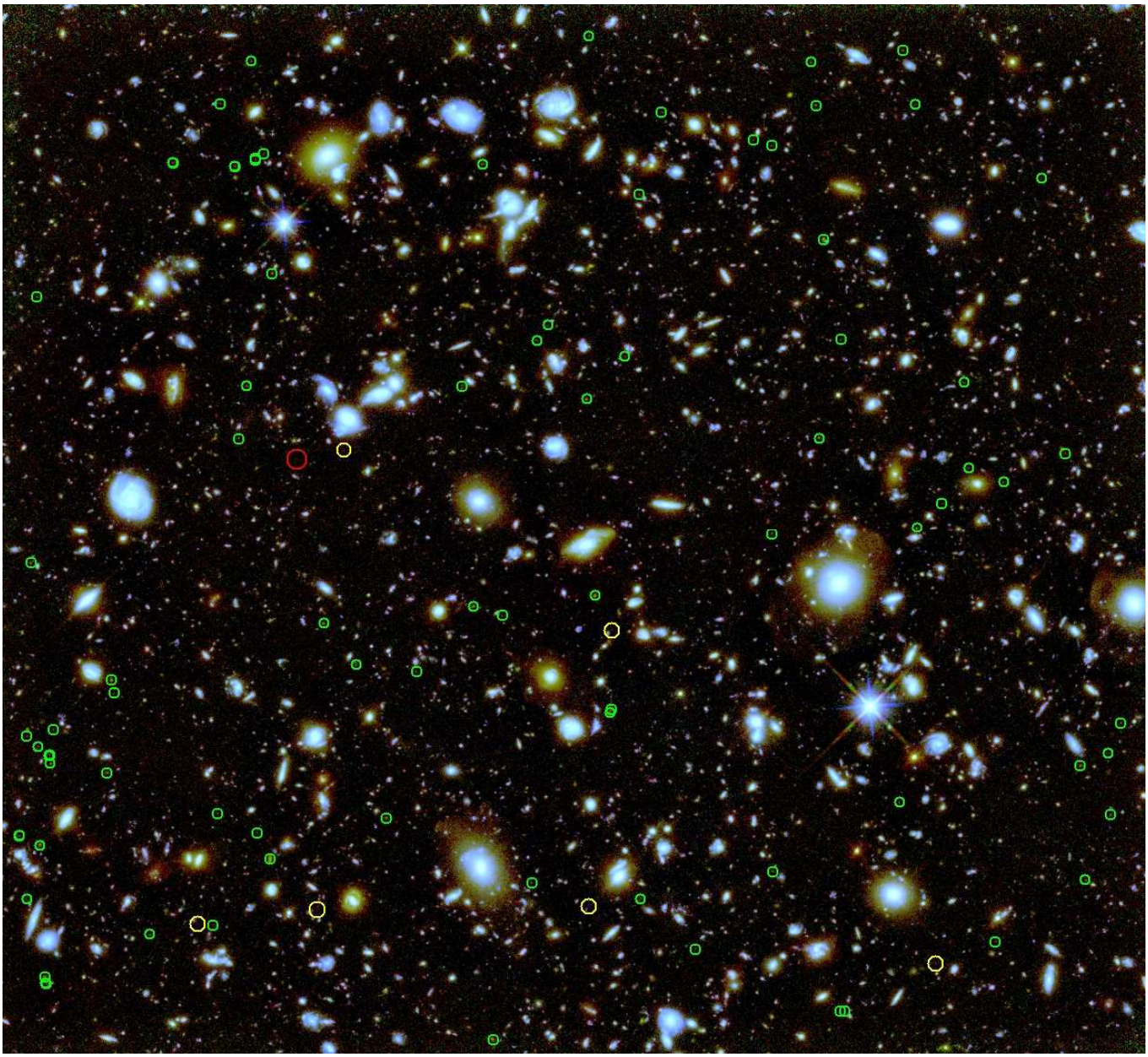

Fig. 1a: The HUDF XDF data from 750 ACS+WFC3 orbits in BViIzYJWH140H (Koekemoer et al. 2013). This image is based on the same data as Illingworth et al. (2012) and Ellis et al. (2013), but displayed at a weighted double log-stretch,. Green circles indicate 76 Lyman-break galaxies at z$\simeq$7–8 (Bouwens et al. 2012; Schenker et al. 2013), yellow circles indicate the six possible dropouts at redshifts z $\simeq$9 (Ellis et al. 2012), and the red circle indicates the only z$\simeq$10–12 galaxy candidate that is common to various authors (Yan et al. 2010; Bouwens et al. 2011; Ellis et al. 2012). Note the enormous drop in surface density between z$\simeq$7–8 and z$\simeq$9–12, which — if real — may indicate a significant drop in M^* at z$\gtrsim$9 (§II & Fig. 4–5). This could trigger the need for gravitational lensing-bias studies of the faint galaxy population at z$\gtrsim$10 with JWST (§III and Fig. 8–11).

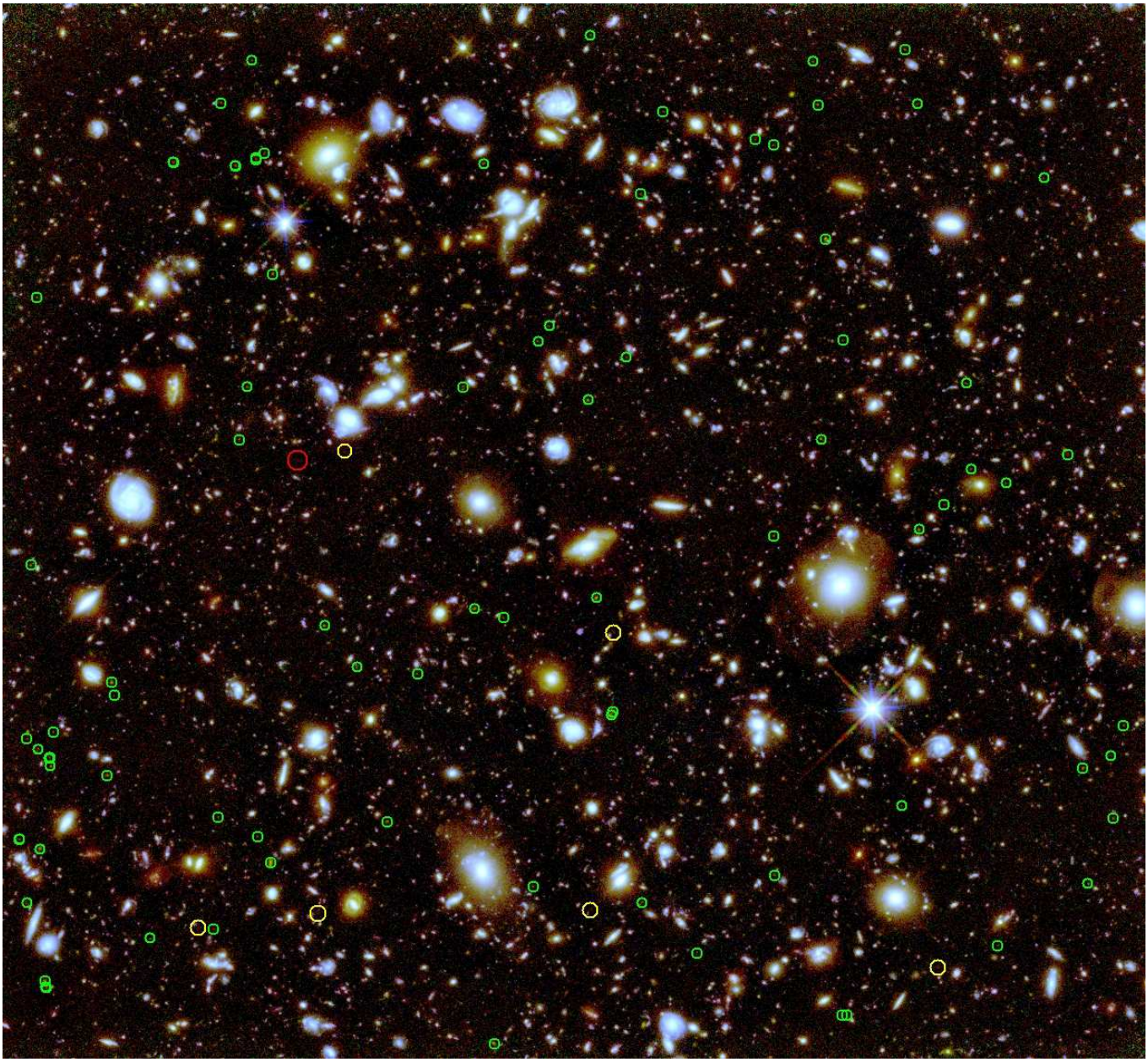

Fig. 1b: Same as Fig. 1a, but displayed with a very hard double log-stretch and color-gray scale, to illustrate fainter features and the possible significant image crowding expected in Webb's (ultra-)deep fields. Residual sky-gradients are $\lesssim 2.4\times10^{-3}$ of sky (or $\gtrsim 29.2$ mag arcsec^{-2}). Sky-gradients in JWST straylight may be 10–20$\times$larger than this (e.g., Fig. 2a–2d), and may be hard to separate from from true object light, unless the field is empty enough to allow making its own sky-flats. [NOTE: The low-level features in this image are best seen when magnifying the PDF file at full-page resolution, with ambient lights off, and blinking between Fig. 1a and 1b.]

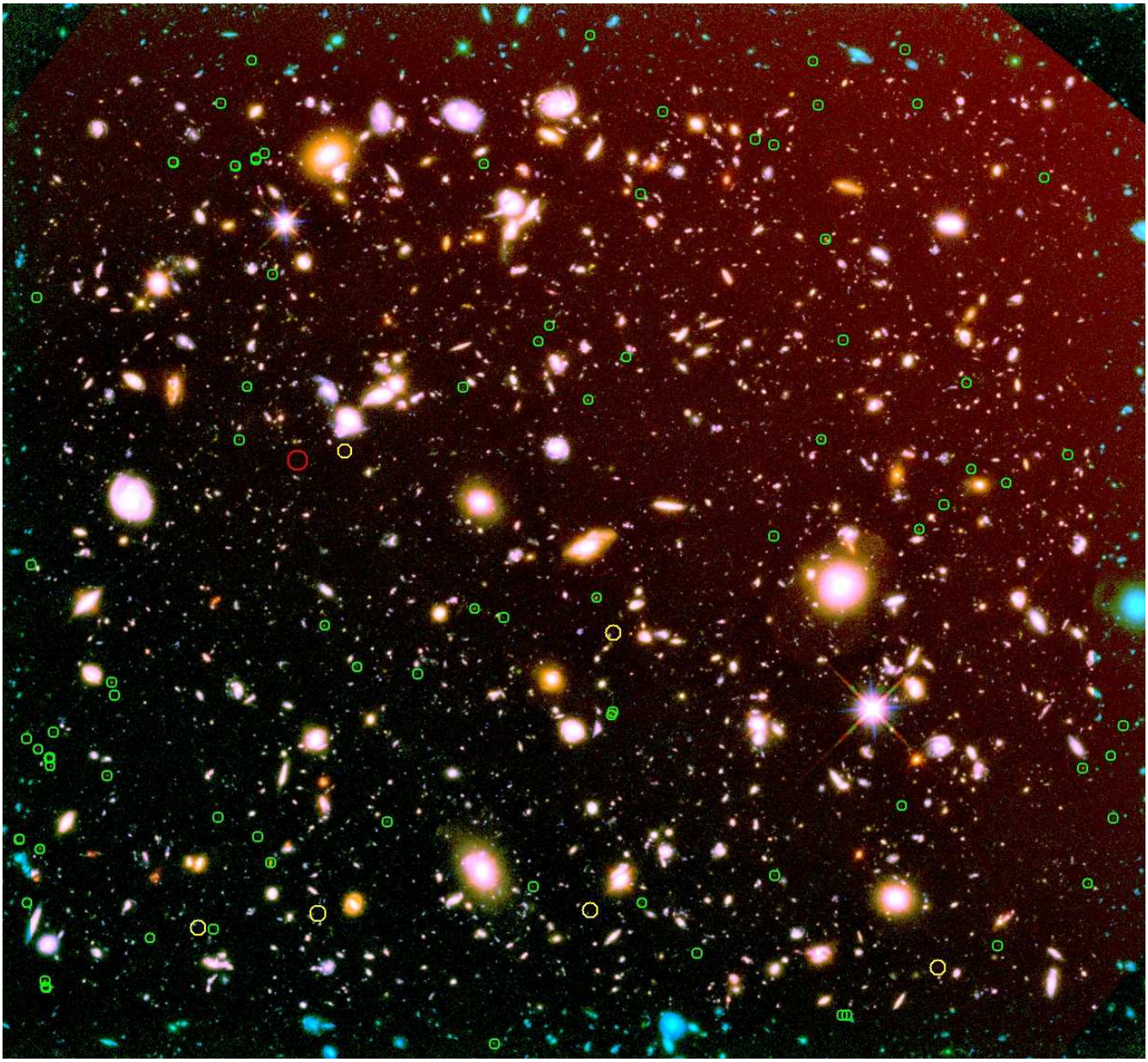

Fig. 1c: The HUDF image with a worst case 95% of Zodi rogue-path amplitude imposed on top of Zodi plus a $\pm$4% *linear gradient* roughly corner-to-corner.

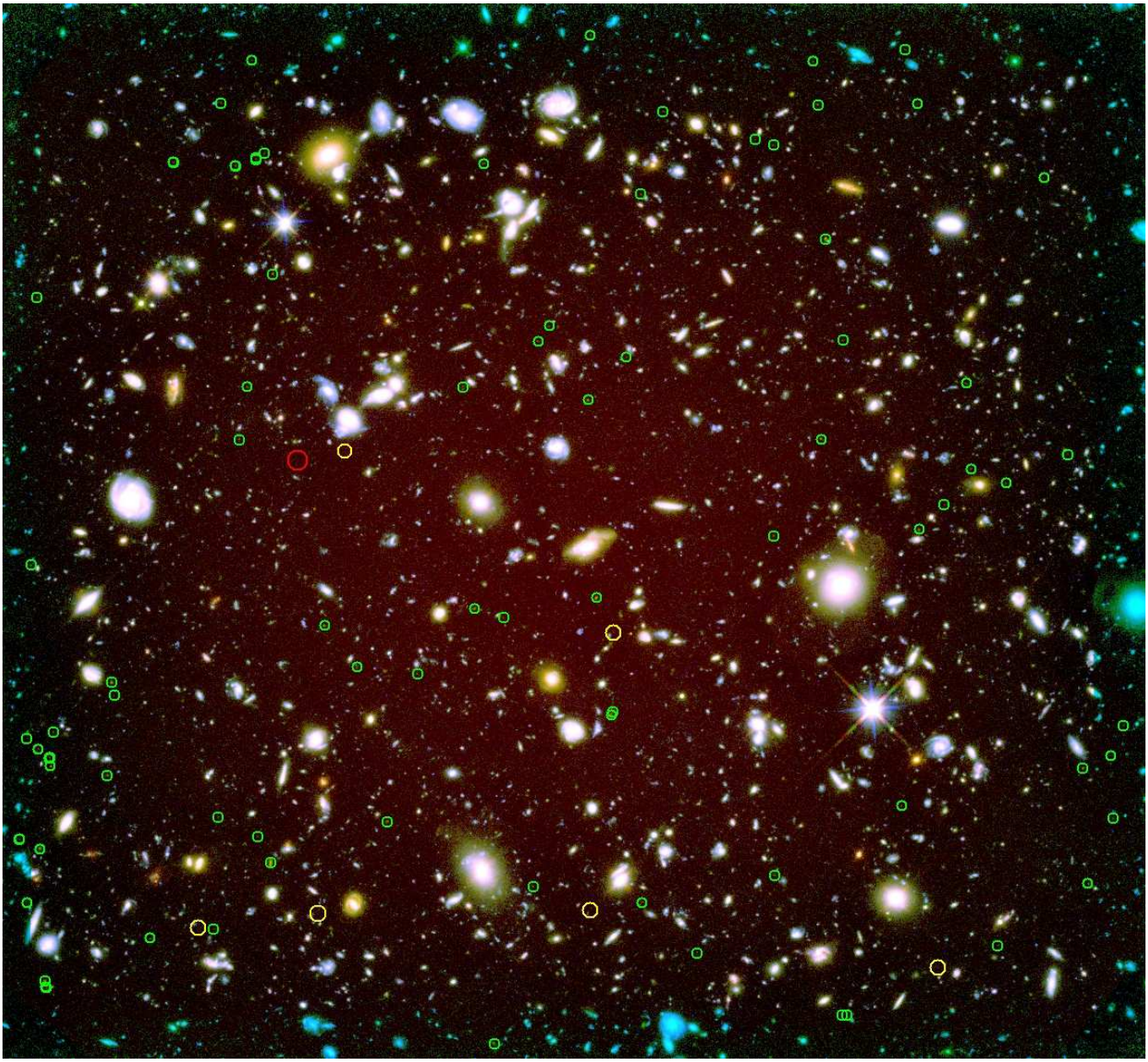

Fig. 1d: The HUDF image with a worst case 95% of Zodi rogue-path amplitude imposed on top of Zodi plus a 4% *single-component 2D spline gradient* superimposed.

Fig. 1e: The HUDF image with a worst case 95% of Zodi rogue-path amplitude imposed on top of Zodi plus a $\pm$4% *2$\times$2-component 2D spline gradient* superimposed.

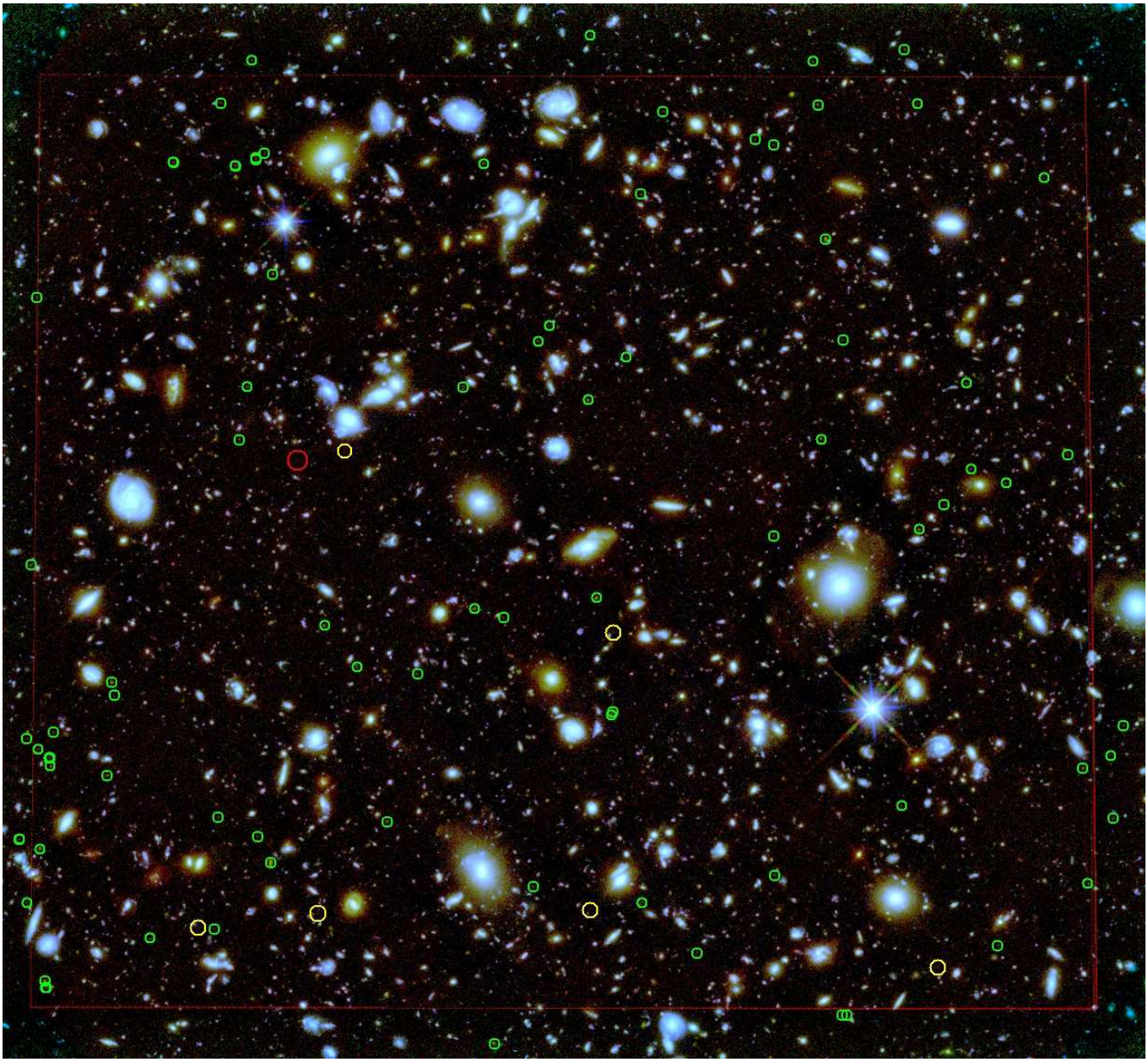

Fig. 1f: The HUDF image with a worst case 95% of Zodi rogue-path amplitude imposed on top of Zodi plus a $\pm$4% 2$\times$2-component 2D spline gradient superimposed, *and after our best effort removal* of the gradient pattern with "rjbgfit.pro". The red box indicates the sky-gradient fitting area used.

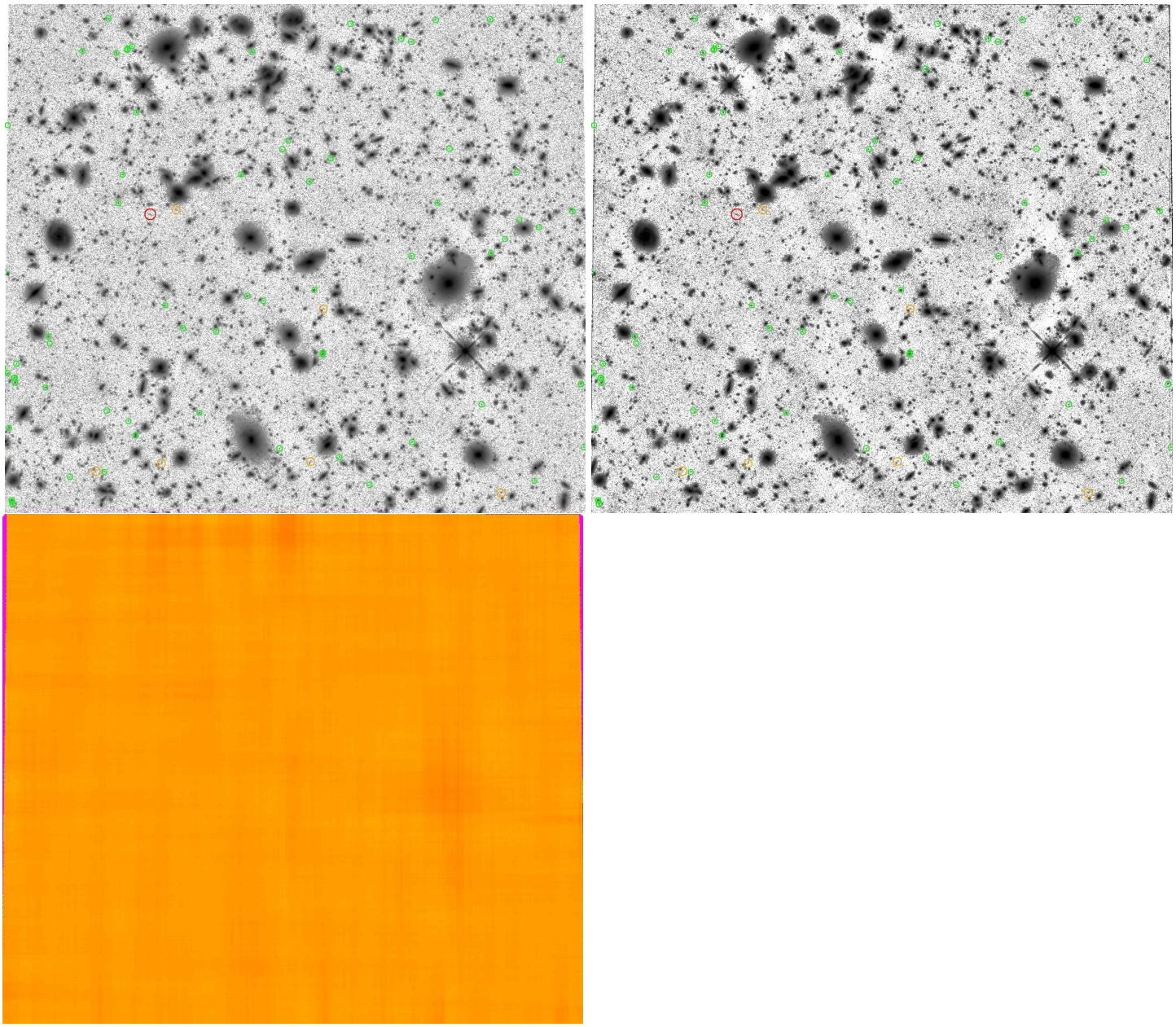

Fig. 2a: [Top Left] HUDF F160W image with *no* rogue-path amplitude imposed on top of Zodi and *no* gradient superimposed; [Top Right] Same image with best fit to sky-background removed; [Bottom Left] Best fit to sky-background with "rjbgfit.pro". In all bottom panels of Fig. 2a–2d, red indicates brighter and yellow indicates fainter surface brightness, with levels varying between $\sim\pm$4% of sky, as listed in Table 1.

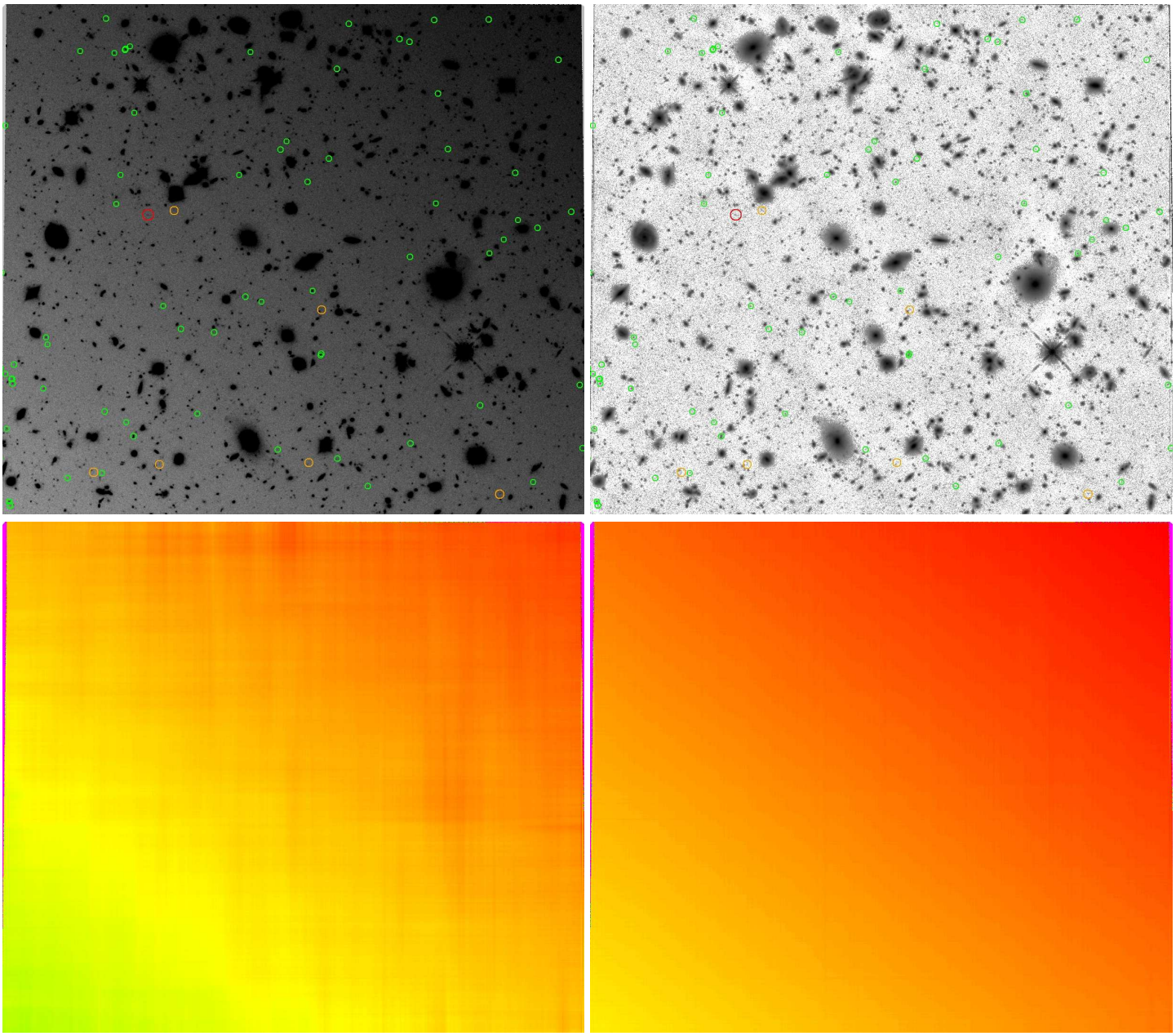

Fig. 2b: [Top Left] HUDF F160W image with a worst case 95% of Zodi rogue-path amplitude imposed on top of Zodi plus a ±4% *linear gradient* roughly corner-to-corner. [Top Right] Same image with best fit to sky-background removed; [Bottom Left] Best fit to sky-background with "rjbgfit.pro". [Bottom Right] Best fit to sky-background with "rjbgfit.pro", with high-frequency structure subtracted (Fig. 2a [Bottom Left]).

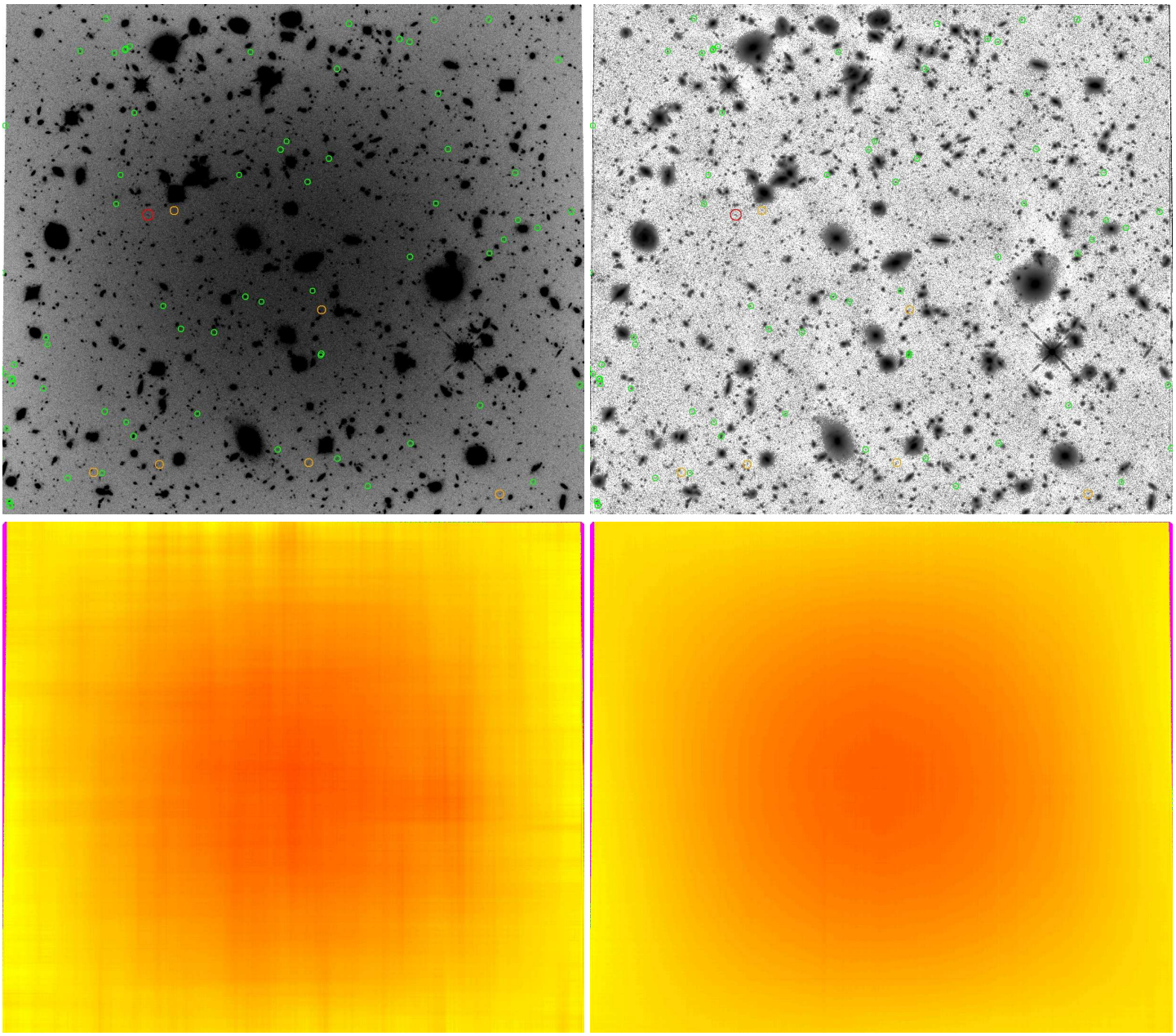

Fig. 2c: [Top Left] HUDF F160W image with a worst case 95% of Zodi rogue-path amplitude imposed on top of Zodi plus a ±4% *single-component 2D spline gradient* superimposed. [Top Right] Same image with best fit to sky-background removed; [Bottom Left] Best fit to sky-background with "rjbgfit.pro". [Bottom Right] Best fit to sky-background with "rjbgfit.pro", with high-frequency structure subtracted (Fig. 2a [Bottom Left]).

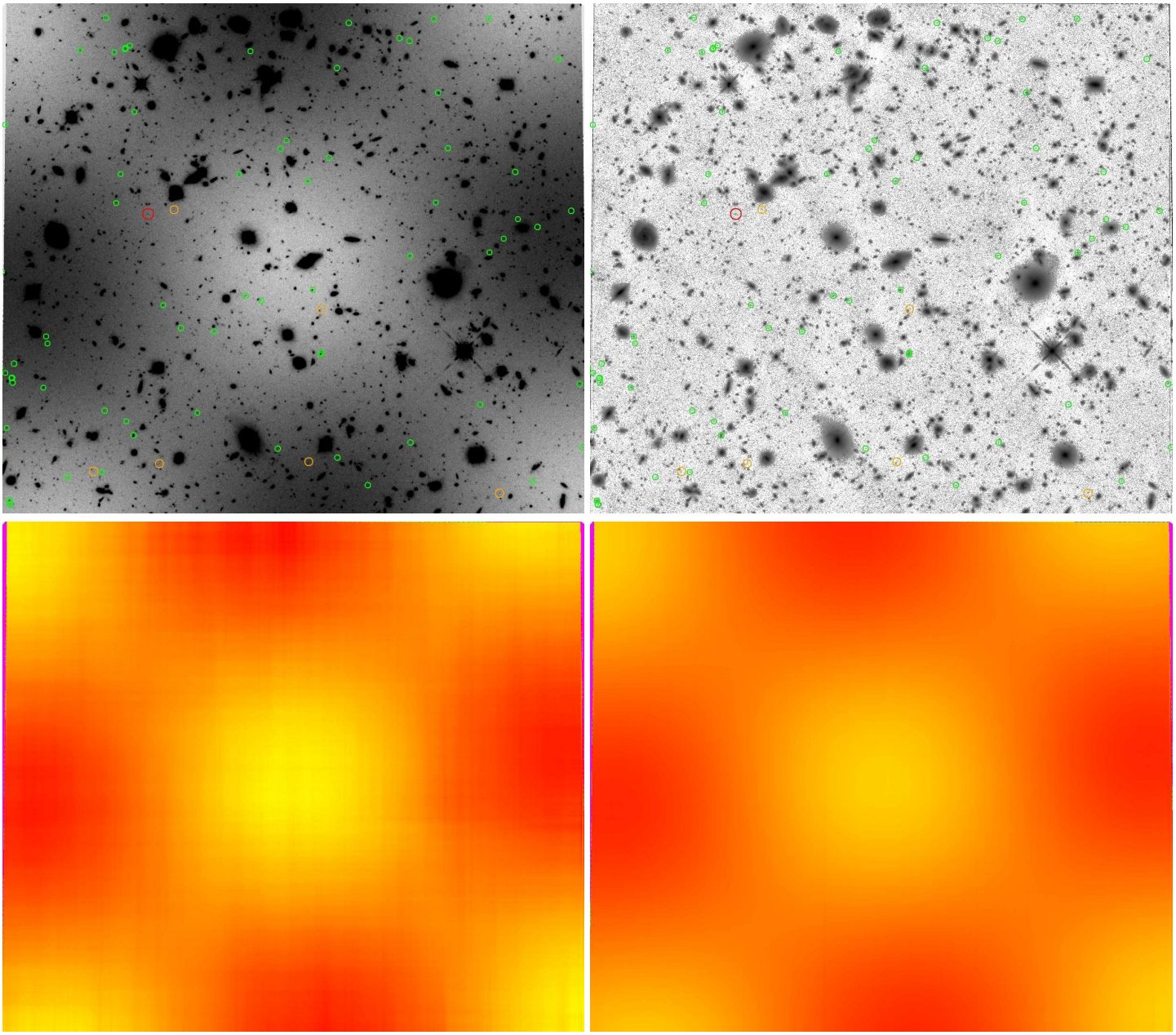

Fig. 2d: [Top Left] HUDF F160W image with a worst case 95% of Zodi rogue-path amplitude imposed on top of Zodi plus a ±4% *2×2-component* 2D spline gradient superimposed. [Top Right] Same image with best fit to sky-background removed; [Bottom Left] Best fit to sky-background with "rjbgfit.pro". [Bottom Right] Best fit to sky-background with "rjbgfit.pro", with high-frequency structure subtracted (Fig. 2a [Bottom Left]).

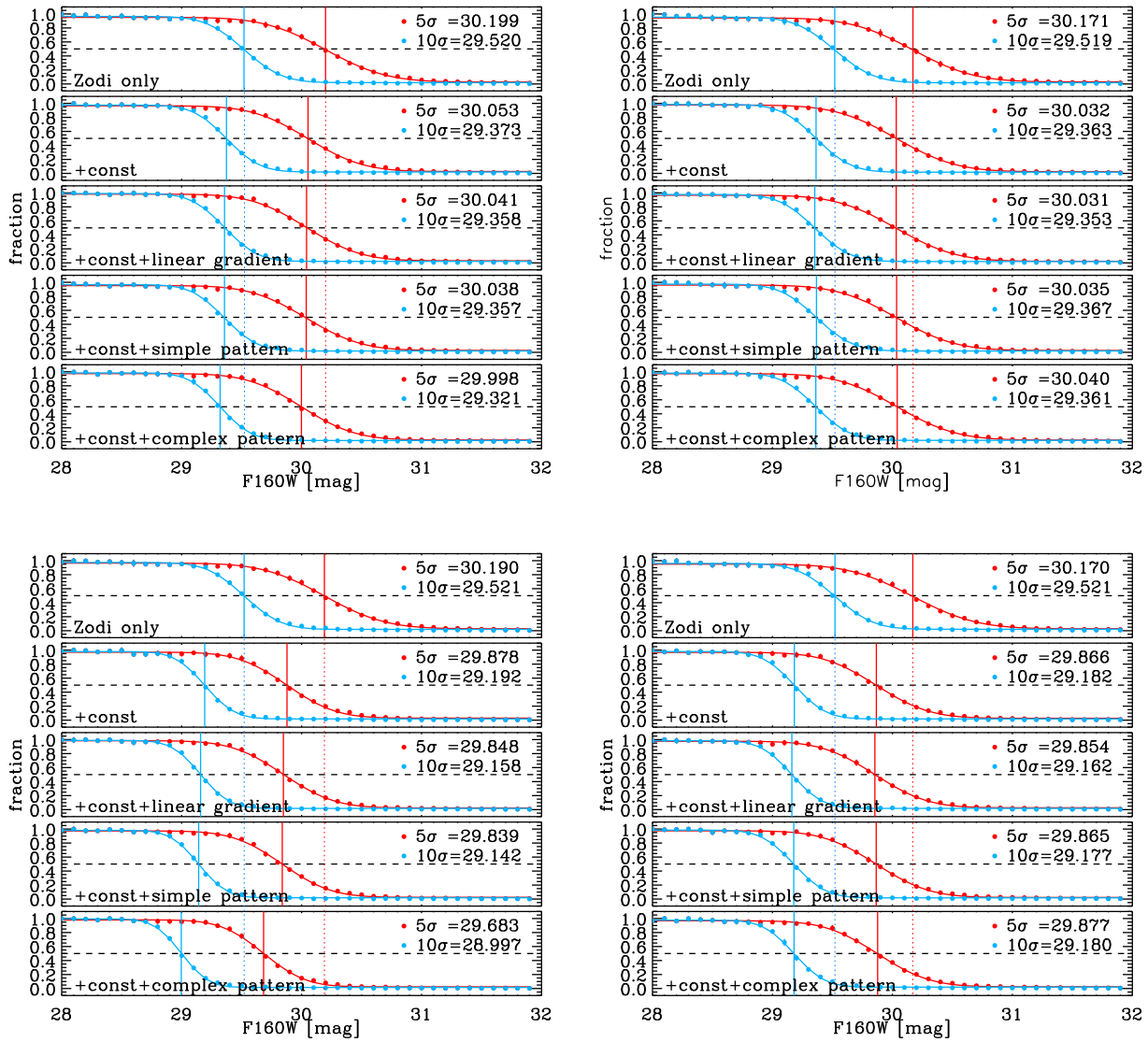

Fig. 3a [TOP 10 PANELS]: Test of completeness of the HUDF F160W image *before* [1st row] the following was also imposed on top of the minimum H-band Zodi (22.70 AB- mag arcsec^{-2} ; Petro 2001): [2nd row] *a constant 35% of Zodi rogue-path amplitude*; OR: [3rd row] *a ±2.5% linear gradient* corner-to-corner; OR: [4th row] *a ±2.5% single-component 2D spline gradient*; OR: [5th row] *a ±2.5% 2×2-component 2D spline gradient*. [LEFT PANELS] SExtractor photometry and measured 50% completeness on above images; and [RIGHT PANELS] Same as left panels *after* the best fit to each image sky-background was made and removed with "rjbgfit.pro". Red and blue lines indicate the 5 and 10-σ detection limits, with the 50% completeness AB-limits listed on the right (see text for discussion).

Fig. 3b [BOTTOM 10 PANELS]: As in Fig. 3a, but using the minimum H-band Zodi [1st row] PLUS: [2nd row] *a constant WORST CASE 95% of Zodi rogue-path amplitude*; OR: [3rd row] *a ±4% linear gradient* corner-to-corner; OR: [4th row] *a ±4% single-component 2D spline gradient*; OR: [5th row] *a ±4% 2×2-component 2D spline gradient*.

2 II. Predicting JWST Number Counts for z$\gtrsim$10 using the HUDF WFC3 IR data

Authors: Seth H. Cohen, Rogier A. Windhorst, Andrew M. Hopkins, Nimish Hathi, & Sadegh Khochfar, others?

2.1 Introduction

Observations of the HUDF with HST/WFC3 have produced many papers on high-redshift galaxy candidates selected via the "dropout" or Lyman-break (LBG) method (e.g., Bouwens et al. 2012, Ellis et al. 2012, Yan et al. 2010). Early papers on the data presented a wide variety of results, due to learning curves about the nuances of the new WFC3, and proper reduction of its data. As of today, there is some consensus on the existence of up to 6 possible z$\simeq$9$\pm$0.5 dropouts, and a single J+F140W-dropout galaxy with a possible redshift of z$\simeq$10.7–11.9 (hereafter "z$\simeq$11"; Bouwens et al. 2012, Ellis et al. 2012; see also Yan et al. 2010; yellow and red circles in Fig. 1a–1e, resp.). Extrapolations of the observed LBG luminosity function (LF) at lower redshift (i.e., z$\simeq$6) predict that several more z$\simeq$10–12 galaxies should have been observed in these XDF data (Oesch et al. 2013). In this paper, we will use this information to explore the possible parameter space for the LF-fit (M^* , α) parameters that the universe presents us here.

2.2 Evolution of Schechter parameters for z$\lesssim$6–8, and extrapolation for z$\gtrsim$8

Fig. 4abc shows the available data on the redshift dependence of the Schechter LF parameters α(z) [top panel], Φ^* (z) [middle panel] and M^* (z) [bottom panel]. The data is summarized in Hathi et al. (2010), and updated with various publications since then, most recently Oesch et al. (2013).

Some hierarchical predictions are also shown. These include GADGET simulations of Morgan et al. (2012, 2013), which were folded with population evolution models, projected onto sky-images at z$\simeq$4.5–10.5 in WMAP cosmology, with the appropriate sky-noise added, and then subject to a similar image analysis as applied to the XDF and JWST images (see e.g. §I). Also shown are recent SPH models by Khochfar et al. (2013), who give detailed predictions of physical parameters and mass functions as a function of cosmic epoch, that can be converted to observed Schechter LF parameters using certain assumptions. These predictions are very useful, although they are hard to make and have their own inherent uncertainties. While the growth and merger-rate of CDM halos is fairly straightforward to compute, in hierarchical models the conversion between these predictions and the actually observed parameters like Schechter α, Φ^* , and M^* is difficult, and subject to many uncertainties, such as the exact star-formation and feedback prescriptions used in the models. Nonetheless, the comparison of detailed model prediction with the data are very useful, and may provide guidance as to what to expect in the redshift range ($\gtrsim$10–12) where we will not have a large amount of data until after JWST is launched and has become operational in late 2018.

In brief, summarizing all available data on the rest-frame UV LF's, the trends of α(z) and Φ^* (z) in Fig. 4a–4b are modest but noticeable. In the intermediate redshift regime (0.5$\lesssim$z$\lesssim$2.5), the error bars are still particularly large, but this will get better as more HST UV surveys are done with the WFC3 UVIS channel of existing HST fields like HUDF, GOODS and CANDELS, which have excellent ACS BViz and WFC-IR YJH images to various depths. In any case, the restframe UV-LF

is well determined by GALEX at low redshifts — we refer the reader here to a discussion of the GALEX UV object count-slope at the bright-end in Windhorst et al. (2011) and papers therein. The resulting best fits of α(z) and Φ^* (z) appear to be slowly varying functions of redshift. The best weighted least-squares *linear* fit over all available α(z) data is as follows (it looks slightly curved as a function of the log(1+z) axis that is plotted in Fig. 4a):

$$\alpha(z \lesssim 8) = -1.27 - 0.085\,z \qquad \text{Eq. (1a)}$$

Hierarchical models suggest that α(z)=–2 for the highest redshifts when structure formation first starts. This is confirmed by, e.g.,, the recent GADGET simulations by Morgan et al. (2013), which are indicated by the long-dashed line in Fig. 4a. The recent SPH simulations by Khochfar et al. (2013; see also Khochfar et al. 2007) similarly suggest a gradual steepening of α(z) with redshift for $z \gtrsim 6$, as indicated by the red dots in Fig 4a [top panel]. Taken together and given the uncertainties in these numbers, it seems reasonable to adopt for $z \gtrsim 8$ a faint-end Schechter slope α that remains roughly constant at:

$$\alpha(z \gtrsim 8) = -2.0 \pm 0.3 \qquad \text{Eq. (1b)}$$

Similar to α(z), all available data for $z \lesssim 8$ seems to suggest that Φ^* (z) is also a slow function of redshift for $z \lesssim 8$, but compared to alpha(z) has a slightly steeper weighted least-squares *linear* slope when fit over all data at $z \lesssim 8$:

$$\log \Phi^*\,(z \lesssim 8) = -2.35 - 0.10\,z \qquad \text{Eq. (2a)}$$

The Press Schechter formalism and hierarchical models make a less iron-clad prediction as to how exactly Φ^* (z) should evolve at the highest redshifts. However, recent SPH simulations by Khochfar et al. (2013) suggest that the trend of Φ^* (z) with redshift for $z \gtrsim 6$ may be mild, as indicated by the red dots in Fig 7. Mindful that the evolution of Φ^* (z) for $z \gtrsim 8$ may in fact be strong — and possibly strongly negative — it seems possible that:

$$\log \Phi^*\,(z \gtrsim 8) \lesssim -3.15 \pm 0.3 \qquad \text{Eq. (2b)}$$

as indicated by the horizontal dotted line in Fig. 4b [middle panel]. Again, we assume that the error on this number is at least a factor of two, given the error bars on the actual fitted data, and the uncertainties present in both the hierarchical model prediction and in the data. To be conservative, we will adopt here:

$$\log \Phi^*\,(z \gtrsim 8) \lesssim -3.0 \qquad \text{Eq. (2c)}$$

In any case, should Φ^* (z) drop more rapidly with redshift than indicated by Eq. (2a, 2b), our numbers predicted below will directly decrease accordingly. The adopted Φ^* ($z \gtrsim 8$)= 10^{-3} Mpc^{-3} is thus conservative, in the sense that the actual numbers may be lower, as long as Φ^* (z) doesn't actually start increasing again with redshift for $z \gtrsim 8$ (which is unlikely in hierarchical models, although perhaps not impossible).

Last but not least, M^* (z) appears to be a stronger, and also a more non-monotonic function with redshift. The three Schechter parameters are strongly correlated as determined in each data set. This is because the the dynamic range in surveys at $z \gtrsim 6$ is generally not large. Also, cosmic variance over the small HST fields can be significant, but may be less so when shallower and

wider-fields HST surveys such as GOODS and CANDELS are included. As a consequence, the LF extrapolation for z$\gtrsim$6 is highly uncertain, especially in M^* (z).

We attempt to capture this by separating the better determined M^* (z) for z$\lesssim$6 from the more uncertain part at z$\gtrsim$6, as follows:

M^* (z$\lesssim$6) = –18.35 –1.427 z +0.2042 z^2 –0.002865 z^3 mag Eq. (3a)

Where we will simply parametrize the M^* (z) for z$\gtrsim$6 as:

M^* (z$\gtrsim$6) = –20.29 + m (z – 6.0) Eq. (3b)

where m symbolizes the rapidity of the decline in M^* (z) for z$\gtrsim$6. Note that a more positive m indicates a more rapid L^* luminosity-decline with redshift, since M^* is in absolute magnitude units. Oesch et al. (2013)'s analysis suggested that:

m = 0.33 (Oesch et al. 2013) Eq. (3c)

The key component in the current paper is that we wish to consider the possibility that m may indicate a steeper L^* -decline than m = 0.33. For instance, the SPH models of Khochfar et al. (2013) — indicated again by red dot in Fig. 4c [bottom panel] — when taken at face value seem to suggest that the M^* luminosity decline with redshift may be as steep as:

$m \simeq$ 1.1 (Khochfar et al. 2013) Eq. (3d)

The best weighted least-squares fit over all available data for z$\lesssim$8 is:

M^* (z$\lesssim$8) = –18.25 –1.6872 z +0.3300 z^2 –0.01787 z^3 mag Eq. (3e)

In the calculations below, it turns out that we actually get a better fit to the z$\lesssim$8 LF if we slightly modify the Oesch et al. (2013) expression in Eq. (3b), so we recommend to use the following:

M^* (z$\gtrsim$8) = –19.77 + μ (z – 8.0) Eq. (3f)

where the different parameter μ now indicates the M^* (z) slope beyond z$\gtrsim$8, where the M^* value may increase more steeply with redshift than in Eq. (3e) implies at z$\lesssim$8, to explain the rapid drop in the number of objects at z$\gtrsim$9–12 in the HUDF/XDF. Below we will argue that with the assumptions above, the six z$\simeq$9 and the single z$\sim$11 candidate thus far detected in the HUDF XDF data imply a suggested best fit value to the currently available data of:

$\mu \simeq$ 0.7 (This paper: upper limit from 1 XDF z$\sim$11 candidate) Eq. (3g)

which is indicated by the orange data point and upper-limit plotted in Fig. 4c [bottom panel]. The two dots on this arrow indicate the change in M^* if Φ^* ranges between the two curves indicated in Fig. 4b.

2.3 Method

We begin with the equations for modeling the observed number counts for a given LF and assumed cosmology (e.g., Gardner 1998). The assumed cosmological parameters adopted are midway between the WMAP year-9 (Hinshaw et al. 2012) and the recent PLANCK values (Planck Collaboration 2013). They are: Hubble constant $H_0 \simeq$68.5 $km\ s^{-1}\ Mpc^{-1}$, matter density $\Omega_M \simeq$0.30, and

Cosmological constant $\Lambda \simeq 0.70$. In order to properly model the observed counts, the equations of e.g., Gardner (1998) are modified to include the (5-$sigma$) completeness function $C(m)$ and the redshift-selection function $S(m, z)$, following Oesch et al. (2013). For the present purposes, the completeness is computed by inserting artificial sources in the HUDF image and computing the recovery fraction of detected objects, as shown in Fig. 3a–3b to test the gradient removal. The redshift selection functions are approximated by a Gaussian function with <z>=9.0 and σ_z=0.5 and <z>=10.7 and σ_z=0.7, as in figure 8 of Oesch et al. (2013).

We use the various equations to compute $n(m)dm$, which is a continuous function of m, the observed 1500Å magnitude, which in this case is the $F160W$-magnitude in the AB system. As galaxies are normally counted in bins of apparent magnitude, we next bin the $n(m)$ function to the desired bin width. All results are presented in units of number per 1.0 magnitude per unit area, which for the HUDF is 4.7 sq. arcmin. In practice, we compute $n(m)$ on a grid that is 10$\times$ finer than the bins over which we will count the galaxies, and use numerical integration to compute the expected number in that bin (using 0.5 mag wide bins). The total number of objects is then just the cumulative sum of the histogram computed for each bin, which converges because we have included the completeness functions explicitly. We have verified the consistency of our models by comparing our LF-predictions to the observed counts of Bouwens et al. (2007) for z$\simeq$4–6 galaxies, and our model predictions lie directly on top of their observed counts.

2.4 Results: Implications from having only one XDF candidate at z$\sim$10–12 for JWST Surveys

Fig. 5abc shows the total expected number of galaxies per magnitude in an HUDF-sized area for each value of (α, M^*), assuming $\Phi^* \simeq 10^{-3}$ Mpc^{-3} as discussed in $ 3.3. The main result here is that the detection of $\lesssim$6 z$\simeq$9 candidates and a single candidate at z$\simeq$10.7 in the HUDF seems to imply that the LF may be significantly evolving from z$\simeq$6 to z$\simeq$10.7, with possibly M^* (z) being as faint as $M^* \simeq$–18.0 to –17.5 at z$\simeq$9 and as faint as $M^* \simeq$–17.0 at z$\simeq$10.7. Note that this is true for any reasonable choice of the faint-end slope in the range –2.3$\lesssim \alpha \lesssim$–1.7, as discussed in §3.3. Of course, the faint-end LF-slope α is not constrained by a $\lesssim$6 candidates at z$\simeq$9 or a single candidate at z$\gtrsim$10. But as shown below, our calculations in Fig. 5a–5b to AB$\lesssim$32 mag are indeed not very sensitive to the actual α value at z$\gtrsim$9, simply because M^* may be fainter than –18.0 mag for z$\gtrsim$9, and therefore the (ultra-)deep surveys may not sample well below M^* , even if they reach AB$\simeq$31–32 mag.

The Bouwens et al. (2011) expression for the evolution of M^* suggests values of $M^* \simeq$–18.7 mag and $\alpha \simeq$–1.73. If these parameters indeed had these values, our calculations (Fig. 5a) would suggest $\sim$8–25 objects at z$\gtrsim$10 in the HUDF, which prediction is significantly more than is actually seen. Therefore, we suggest that the LF at z$\gtrsim$9 may be evolving strongly, with either M^* or Φ^* dropping rapidly with increasing redshift, or possibly a combination of both.

Fig. 5a shows the results from our XDF number density predictions, using the relations of α(a), Φ^* (z) and M^* (z) from Fig. 4abc, as explained in detail in §3.3. The Schechter LFs were integrated for three possible cases of JWST surveys:

• (1) A Webb "Medium-Deep" Field or **WMDF** with a survey depth of $J_{AB} \lesssim$30 mag, requiring typical $\times$2 hr integrations in 3–4 NIRCam filters each [Fig. 5a; Left Panel]. For wavelengths $\lesssim$1.7μm, this is also roughly the HST WFC3 XDF limit.

• (2) A Webb Deep Field or **WDF** with a survey depth of $J_{AB} \lesssim 31$ mag (4×25 hrs with NIRCam) [Fig. 5b; Middle panel], and and

• (3) A Webb UltraDeep Field or **WUDF** with a survey depth of $J_{AB} \lesssim 32$ mag (4×150 hr NIRCam) [Fig. 5c; Right panel]. Such a ultradeep JWST survey may cost more 850 hours, taking the nominal 70% JWST spacecraft efficiency into account, and it may not get done during the first year after JWST's launch.

We assume throughout that JWST surveys will be exposing in at least 7 broad-band filters with the 4 filters in the SWC and 3 filters in the LWC filter exposed simultaneously).

A main conclusion of this paper is that UltraDeep JWST surveys to AB$\lesssim$32 mag must be done before the end of its life-time, and the calculations below further illustrate why they must be done.

Correcting for the fact that the sky to AB$\lesssim$30 mag is ∼45% covered by (the outskirts of) foreground objects (Koekemoer et al. 2013; Windhorst et al. 2008), at most 6 z≃9±0.5 candidates and one z≃11±1 candidate are detected in the *actual HST/WFC3 XDF* to AB=30 mag (Bouwens et al. 2012, Ellis et al. 2012; the 6 yellow and one red circle in Fig. 1a–1e). Cosmic variance over the small HST and JWST fields-of-view can change this number by a factor of $\gtrsim$1.3–1.5 (Somerville et al.2004). Hence, we will adopt uncertainties in the number density implied by this one detected candidate of at least a factor of 3, as indicated by the large error flags on the data point and upper limits in Fig. 4c [bottom panel; (in orange)] and Fig. 5a–5c (in black).

For any reasonable value of α(z) close to –2.0 at z$\gtrsim$10 (Fig. 4a and §2.3), this small number of XDF detections — given its significant uncertainties — then implies that the Schechter M^* values at z$\gtrsim$9–11 may be as faint as $M^* \gtrsim$–18.0 to –17.0 mag, respectively, as indicated by the black arrows in the three panels of Fig. 5a–5b. The right two panels in Fig. 5a–5b are the z≃9 and z∼10–12 objects counts expected in deep (AB$\lesssim$31 mag) and ultradeep (AB$\lesssim$32 mag) JWST surveys that cover the FOV of a *single* NIRCam LW detector, which covers about the same area as the XDF (4.7 arcmin^2). Note that the actual JWST NIRCam FOV is about twice as large at 9.2 armin^2, since it covers two independent channels *simultaneously*, so the actual number of objects detected by JWST is expected to be twice as large as the colored number scale of Fig. 5a–5b indicates. These calculations were done by integrating over the Schechter LF with (M^* , α) values as indicated along the axes, using a completeness function C(m) that goes 1–2 mag fainter, to represent the anticipated cases of the WDF (AB$\lesssim$31 mag) and the WUDF (AB$\lesssim$32 mag), respectively.

For the record, it is reasonable to extrapolate the Schechter LF with the same faint-end slope α(z) to some rather faint absolute magnitude , as long as the integral converges. This can be made plausible from what we know at lower redshifts. The WFC3 J- and H-band galaxy counts have a faint-end mag-slopes ≃ 0.12±0.02 to AB$\lesssim$30 mag, when the counts are carried out on the XDF images (see Fig. 12i–12j of Windhorst et al. 2011; shown here in Fig. 6ab with the new XDF counts added). At this very faint flux level, the integrated J+H-band counts reach a surface density ∼2×10^6 galaxies per deg^2. At the median redshift of the faint galaxy population (z_{med} ≃1.6), this faint-end mag-slope of the counts corresponds to a faint-end LF-slope of α≃–1.3 at z_{med} ≃1.6, within the errors consistent with the α≃–1.4 value that Fig. 4a implies for z≃1.6. To AB$\lesssim$30 mag, the faint-end of the LF at z_{med} ≃1.6 thus probes objects as faint as M$_{AB}$≃–14 mag (see also the cluster lensing studies of Siana et al. 2012, which reach at least as faint). The observed faint-end mag-slope of the XDF J- and H-band counts in Fig. 6ab thus suggests that it is possible that the LF continues with a power-law faint-end slope to luminosities at least 6 mag below the break in the

LF (*i.e.*, , $M_{AB}\simeq$–14 mag compared to M^* ($z_{med}\simeq$1.6) $\simeq$–20 mag; see Fig. 4c bottom panel). We will use this indirect argument here justify integrating the faint-end of the LF at $z\gtrsim 10$ as a power law that may continue to rather faint luminosities (*i.e.*, $M_{AB}\simeq$–15 mag or fainter). Fig. 6ab also shows the AB$\lesssim$30 mag limit of the XDF, as well as the AB$\lesssim$30, 31, 32 mag limits (in orange) for the WMDF, WDF, and WUDF, respectively, plus the lensing limit for the WUDFF (in red). The effective 150 hr JWST limit of AB$\lesssim$32 mag is equivalent to M$\simeq$–15.5 mag at z$\simeq$11, so we are not integrating to unreasonably faint luminosity limits for star-forming objects that are not seen at lower redshifts.

The total number of detected objects in each (M^* , α) bin in Fig. 5abc is indicated by the color scale to the right. As consistency check, our numerical integration confirms that — assuming M^* $\simeq$–17.0$\pm$0.75 mag and $\alpha\simeq$–2.0$\pm$0.3 — only 6–18 objects at z$\simeq$9$\pm$0.5 and 1–3 objects at z$\simeq$11$\pm$1 are predicted to the XDF detection limit of AB$\lesssim$30 mag, confirming the input of our calculations above. Similarly, our numerical integration also confirms the calculations of Oesch et al. (2013) that *if* $\alpha\simeq$–1.73 and *IF* M^* remains as bright as $\simeq$–18.6 mag at z$\simeq$11, then the XDF should have seen 15–25 candidates at z$\simeq$10–12, while we detect only one.

2.5 Specific Predictions for JWST Medium Deep, Deep and UltraDeep Surveys

Fig. 7abc present the Press Schechter prediction of the galaxy LF for $z\lesssim 6\lesssim 20$ using the α(z), Φ^* (z), and M^* (z) relations of Fig. 4abc. The possible redshift evolution of these Schechter parameters is captured by the 3 indicated parameter values as discussed in §2.2, Eq. (3a)–(3g), and as illustrated in Fig. 4abc. The Schechter LF gives predictions as a function of M_{AB} (in mags) and space density ρ(M) (in Mpc) as indicated by the black axes at the top and on the right, respectively. The corresponding *observed* quantities are m_{AB} and the number density N(m), respectively, and are indicated along the purple bottom and left axes, respectively. These curves are only exact for z=6 (purple), but we shifted the other colored curves to be approximately correct for $z\gtrsim 7$ as well, using our adopted WMAP9/Planck13 cosmology. (As a consequence, the black M_{AB} and ρ axes are only correct for z=6, and are shifted by, e.g., $\sim$+0.78 mag and –0.3dex at z$\simeq$10) — this does not affect the current discussion in any major way). The HUDF/XDF field-of-view and detection limit are indicated by the horizontal and vertical lines respectively. Similar lines are shown for HST GOODS in purple and for the various JWST surveys in orange. The latter are: the Webb Medium Deep Survey (10 WMDF pointings), the Webb Deep Field (2 WDF pointings are assumed), and the Webb UltraDeep Field (1 WUDF pointing). For the 10 WMDF and 1 WUDF pointings, the red wedge indicates the gain obtained in sensitivity due to gravitational lensing, if these are pointed at foreground clusters or rich groups with significant compactness. The (lensed) Webb deep fields will be able to find "first light" objects to $z\lesssim 13$ (to $z\lesssim$15–16 when lensed), but such objects may be quite rare if the HUDF is representative enough for the above predictions.

Fig. 7b shows the same as Fig. 7a, but with the M^* (z) evolution parameter set to μ=0.33, as in Oesch et al. (2013). This shows that the M^* ($z\gtrsim 8$) behavior in Fig. 4a cannot continue to decline with redshift as slowly as it does for $3.5\lesssim z\lesssim 8$, or far more objects at $9\lesssim z\lesssim 12$ would have been seen in the XDF, even though the number of objects at $6\lesssim z\lesssim 8$ remains roughly the same as in Fig. 7a. Instead, as we suggest in Fig. 4c, 5a, and 7b, M^* (z$\simeq$9) is likely fainter than –18.0$\pm$0.5 mag, and M^* (z$\simeq$11) is likely fainter than –17.5$\pm$0.5 mag.

Fig. 7c shows the same as Fig. 7b, but with the M^* (z) evolution parameter set to μ=1.00,

which is still allowed by the data in Fig. 4c. Such large values of μ produce a significant decline in M^* for z$\gtrsim$8. As a consequence, the LF at z$\gtrsim$8 would drop dramatically and result in far fewer high redshift objects expected for JWST at z$\gtrsim$12–13. The only other data added here are the upper limits to the z$\simeq$6 quasar host galaxy fluxes by Mechtley et al. (2012, 2013). The blue dot indicates their one possible host galaxy detection (Mechtley et al. 2013). The epoch dependent LF of quasars was not done with the Schechter prescription, and is only intended to illustrate the possible co-evolution of supermassive blackholes in AGN and that of massive galaxies, which *was* computed one with the Schechter prescription. The QSO LF at z=6 was normalized to the known surface density of SDSS and other z=6 quasar surveys (Jiang et al. 2008, 2009).

2.6 Discussion and Conclusions

In conclusion, the small number of actual z$\sim$10–12 detections in the WFC3 XDF may imply that M^* drops significantly to $M^* \simeq$–17.5$\pm$0.75 mag at z$\simeq$9 and to $M^* \simeq$–17.0$\pm$0.75 mag at z$\gtrsim$11, and/or that Φ^* similarly drops at z$\gtrsim$9–11. This then implies that JWST with NIRCam's full FOV may detect $\lesssim$15–50 objects at z$\simeq$10–12 to AB=31 mag in Webb Deep Fields, and 60–180 objects to AB$\lesssim$32 mag in Webb UltraDeep fields. Depending on how rapidly M^* (z) and Φ^* (z) actually decline with redshift at z$\lesssim$12, the number of objects detected in JWST (UltraDeep) surveys *at higher redshifts* **may be smaller still.**

Another consequence of this result is that it may be necessary to carry out medium-deep JWST surveys on the appropriate foreground lensing targets, to maximize the number of objects detected in reasonable amounts of JWST time, since they will likely mostly survey the LF at levels brighter than M^* at z$\gtrsim$10, and therefore may not see many objects, unless gravitational amplification from known foreground lenses is used.

Last, we consider it critical that more detailed hierarchical models are run over sufficiently large volumes, with sufficient mass resolution — and the appropriate amount of star-formation physics and feedback included — so that a more accurate theoretical prediction can be made of the run of α(z), Φ^* (z), and perhaps most importantly, of the more strongly varying M^* (z) behavior with redshift. Like the Khochfar et al. (2013) simulations have done, such models will provide critical guidance for planning the optimal mix of JWST surveys of the "first light" epoch, in terms of area and depth.

2.7 Future work in FY14 and beyond

(1) For the next steps, we will use our numerical integration to place constraints on the evolution of Schechter parameters at lower redshifts (i.e., z$\simeq$7–8), where we have more than one plausible candidate, so that we can use the slope of the observed counts at these redshifts to constrain the shape and faint-end slope of the LF. We will then refine our computations of what to expect from Webb's MDF, DF, and UDF observations, and compare these to the predictions of state-of-the-art hierarchical galaxy formation models.

(2) We also plan to investigate the effects of more significant image crowding, *i.e.*, , natural confusion. We intend to assess this with more detailed Monte Carlo insertions as in Fig. 3–3b.

Acknowledgements: We thank Sadegh Khochfar for helpful discussions regarding his models

before publication. This work was supported by NASA JWST Interdisciplinary Scientist grant NAG5-12460 from NASA Goddard Space Flight Center.

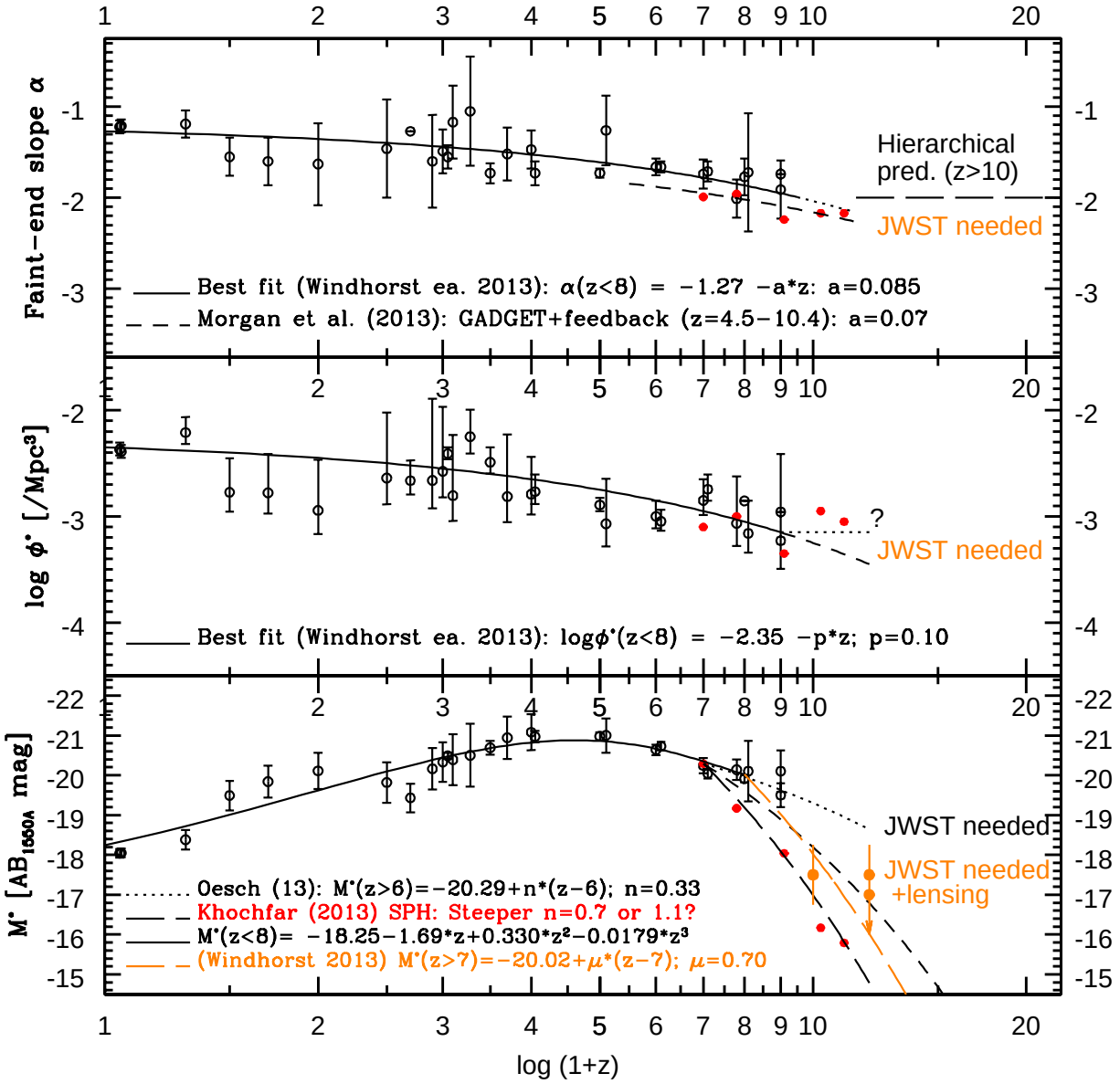

Fig. 4abc: Available data on the redshift dependence of the Schechter LF parameters: α(z) [top panel], Φ^* (z) [middle panel] and M^* (z) [bottom panel], with some hierarchical predictions as indicated. Most of these samples are LBG selected, although some studies supplemented the Lyman break selection work with photometric redshift determinations for the dropout candidates. In this figure, α(z) shows mild steepening with redshift for z$\lesssim$8, and Φ^* (z) a mild but noticeable decrease with redshift, while M^* (z) shows a more significant and non-monotonic behavior. For the calculations of what JWST may expect at z$\gtrsim$10, we adopt α(z$\gtrsim$8) = –2.0, logΦ^* (z$\gtrsim$8)$\lesssim$–3.0, and three different scenarios for M^* (z$\gtrsim$8), as outlined here and discussed in the text. The best fit to the XDF data at z$\gtrsim$10 in Fig. 5a and 7a is obtained if M^* (z$\simeq$11) is fainter than –17.5$\pm$0.5 mag.

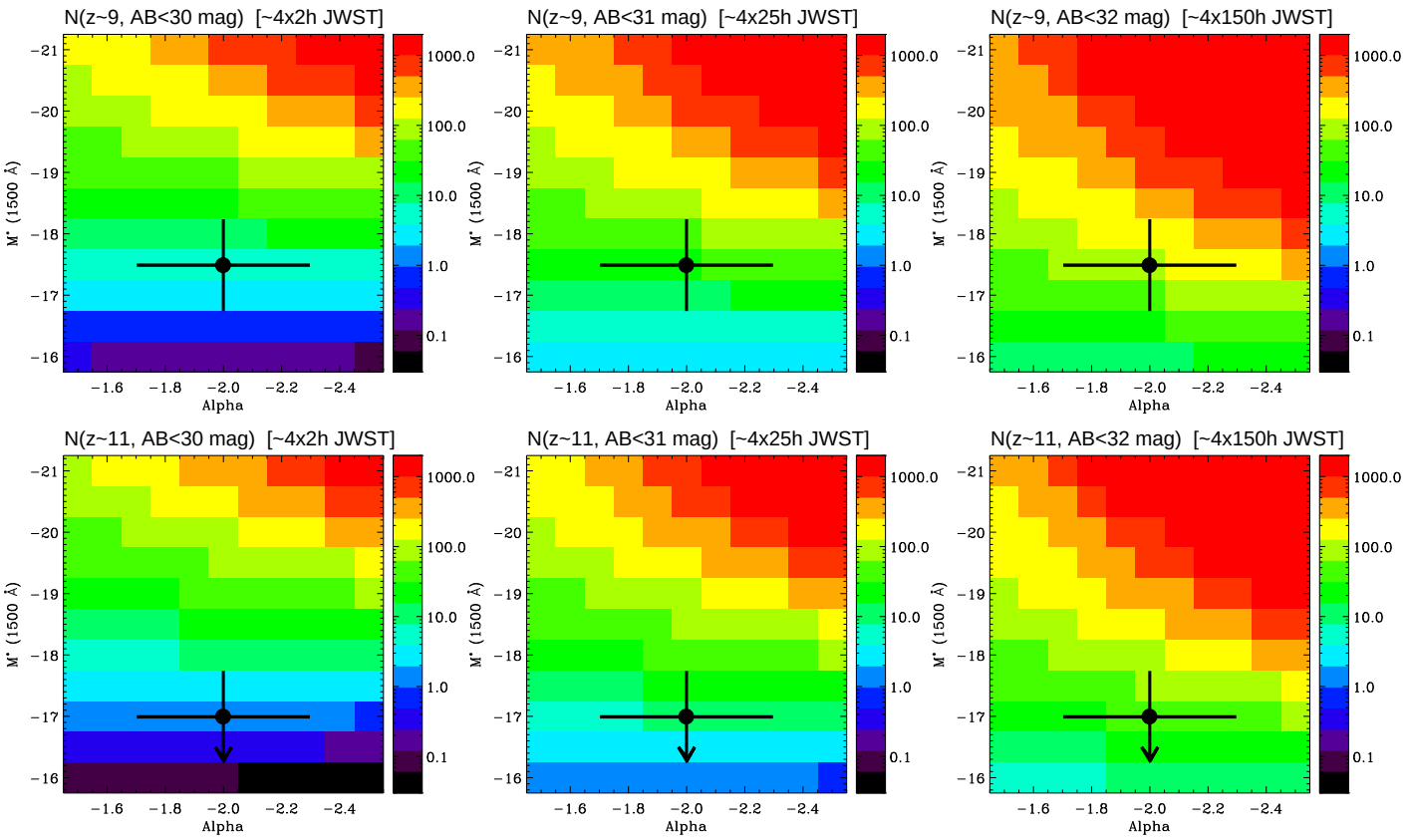

Fig. 5a [TOP panels]: Count model for z≃9±0.5 with the α(z), Φ^* (z) and M^* (z) relations described in Fig. 4abc. Fig. 5a [BOTTOM panels]: Same as Fig. 5a, but for z≃11±1. All Schechter LFs were integrated to:

(1) The HST WFC3 XDF limit of $J_{AB} \lesssim 30$ mag [Left Panel], which is also the Webb "Medium-Deep" Field or **WMDF** survey limit (typical ∼2 hr integrations in 3–4 NIRCam filters each);

(2) The Webb Deep Field or **WDF** survey limit of $J_{AB} \lesssim 31$ mag (4×25 hr) [Middle panel]; and

(3) The Webb UltraDeep Field survey limit of $J_{AB} \lesssim 32$ mag (4×150 hr) [Right panel].

Correcting for the fact that the sky to AB$\lesssim$30 mag is ∼45% covered by (the outskirts of) foreground objects (Koekemoer et al. 2013; Windhorst et al. 2008), only 6 (±0.5dex) candidates at z=9±0.5 are detected in the *actual HST/WFC3 XDF* to AB=30 mag, and only one candidate at z=11±1 (Bouwens et al. 2012, Ellis et al. 2012; 6 yellow circles and one red circle in Fig. 1a–1b). For any reasonable α(z) at z$\gtrsim$9–11 (Fig. 4c), this number of detections then implies that the Schechter M^* values at z∼9 may be as faint as –17.5 mag at z≃9, and faint as –17.0 mag at z≃11, as indicated by the black data points and upper limits here. The right two panels are the objects JWST counts expected for the WDF and WUDF, using a power-law extrapolation of the Schechter LF using (M^* , α) values as indicated along the axes. The total number of detected objects in each (M^* , α) bin is indicated by the color scale to the right of each box.

The number of actual z≃9 and z≃11 candidates in the WFC3 XDF implies that JWST NIRCam may detect $\lesssim$60–180 objects at z≃9 to AB$\lesssim$31 mag in the WDF, and 210-600 z≃9 objects to AB$\lesssim$32 mag in the WUDF, and 15–50 objects at z≃11 to AB$\lesssim$31 mag in the WDF, and 60–180 z≃11 objects to AB$\lesssim$32 mag in the WUDF. For higher redshifts (z≃11–15), we believe that it may be necessary to carry out Webb's Medium-Deep Field surveys ($\lesssim$4×2 hrs) primarily on the appropriate foreground lensing targets such as compact groups and rich clusters, to maximize the number of objects actually detected in reasonable amounts of JWST time.

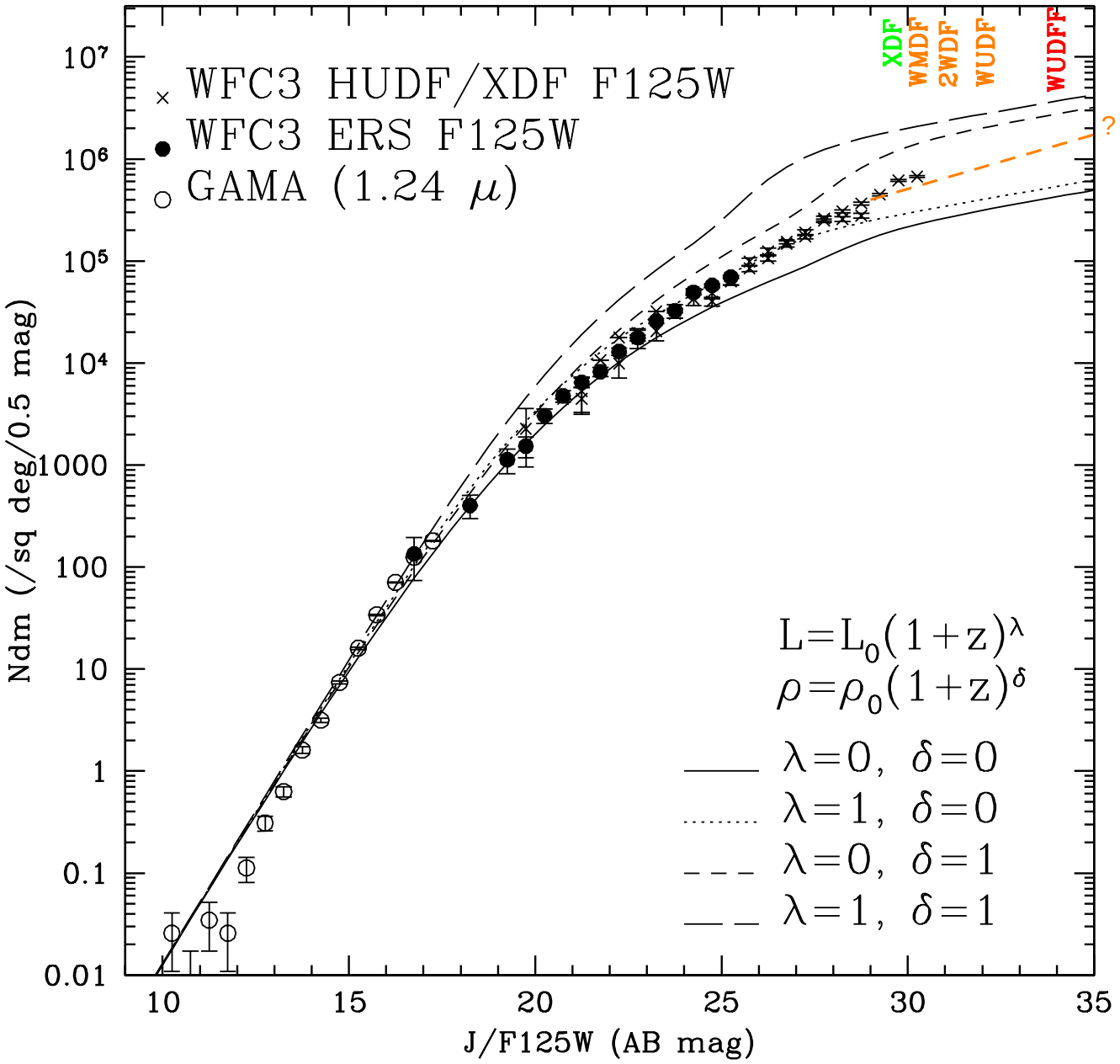

Fig. 6a: Differential galaxy number counts for the entire flux range AB=10–30 mag in the WFC3 filter F125W (J). For details on data and the simple count models, see Windhorst et al.(2011). In brief, the bright-end of the counts (AB$\lesssim$18 mag) come from the GAMA survey (Driver et al. 2009), the intermediate flux-range (18$\lesssim$AB$\lesssim$26 mag) from the HST/WFC3 ERS (Windhorst et al. 2011), and the faint end (24$\lesssim$AB$\lesssim$30 mag) from the HUDF XDF data (Bouwens et al. 2012, Ellis et al. 2012; see also Yan et al. 2010). The counts roughly have a power-law faint-end with mag-slopes $\simeq$0.12$\pm$0.02 for 14$\lesssim$AB$\lesssim$30 mag. The orange dashed line is the extrapolation expected for JWST, and falls roughly between the 2nd and 3rd model. Also shown are the AB$\lesssim$30 mag limit of the XDF, as well as the AB$\lesssim$30, 31, 32 mag limits for the WMDF, WDF, and WUDF, respectively, plus the lensing limit for the WUDFF (AB$\lesssim$34 mag). The faint counts sample on average the galaxy population with a median redshift z_{med} $\simeq$1–2, sampling, reaching $\sim$6 mag fainter than M^* at z$\simeq$1.6.

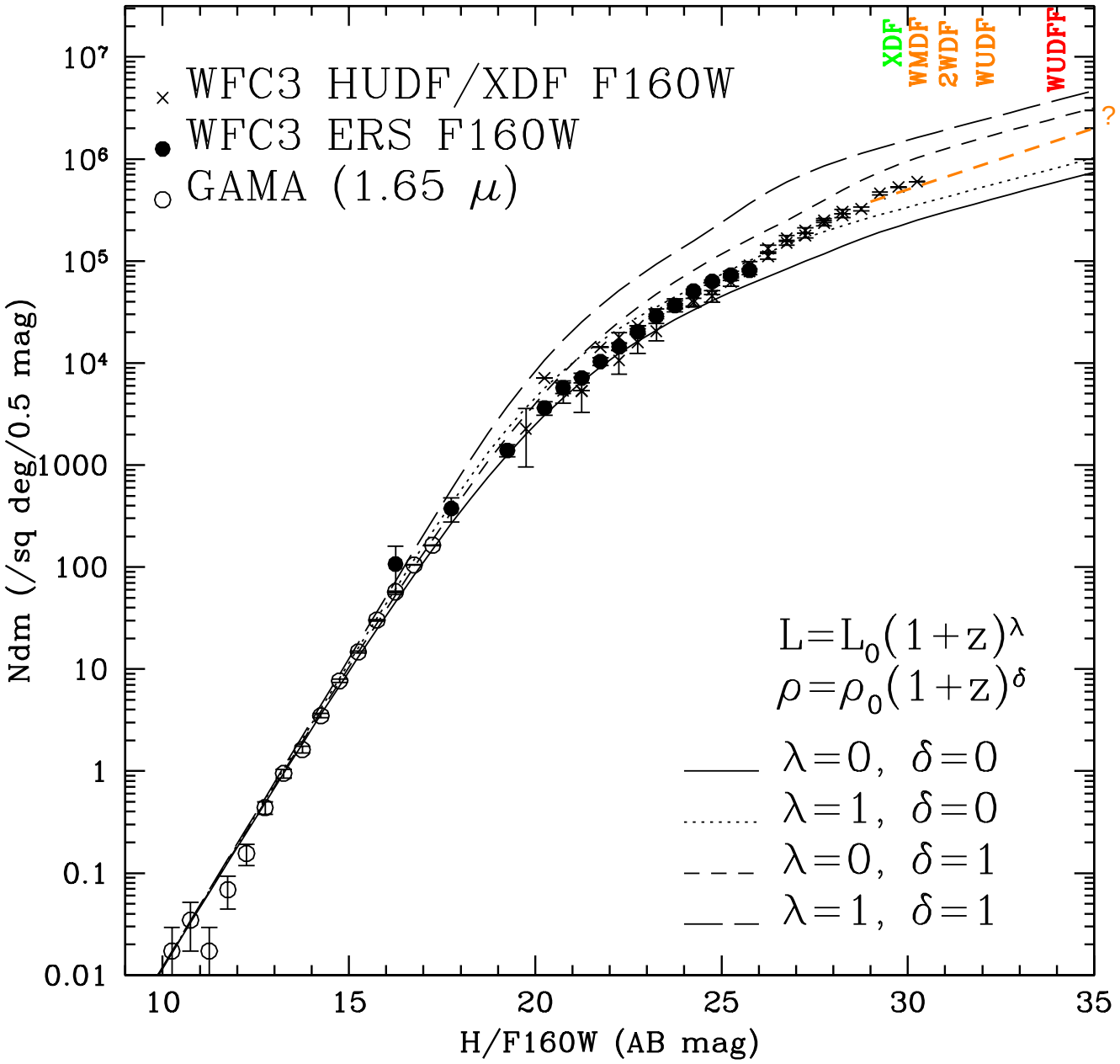

Fig. 6b: Same as Fig. 6a but for the WFC3 filter F160W (H).

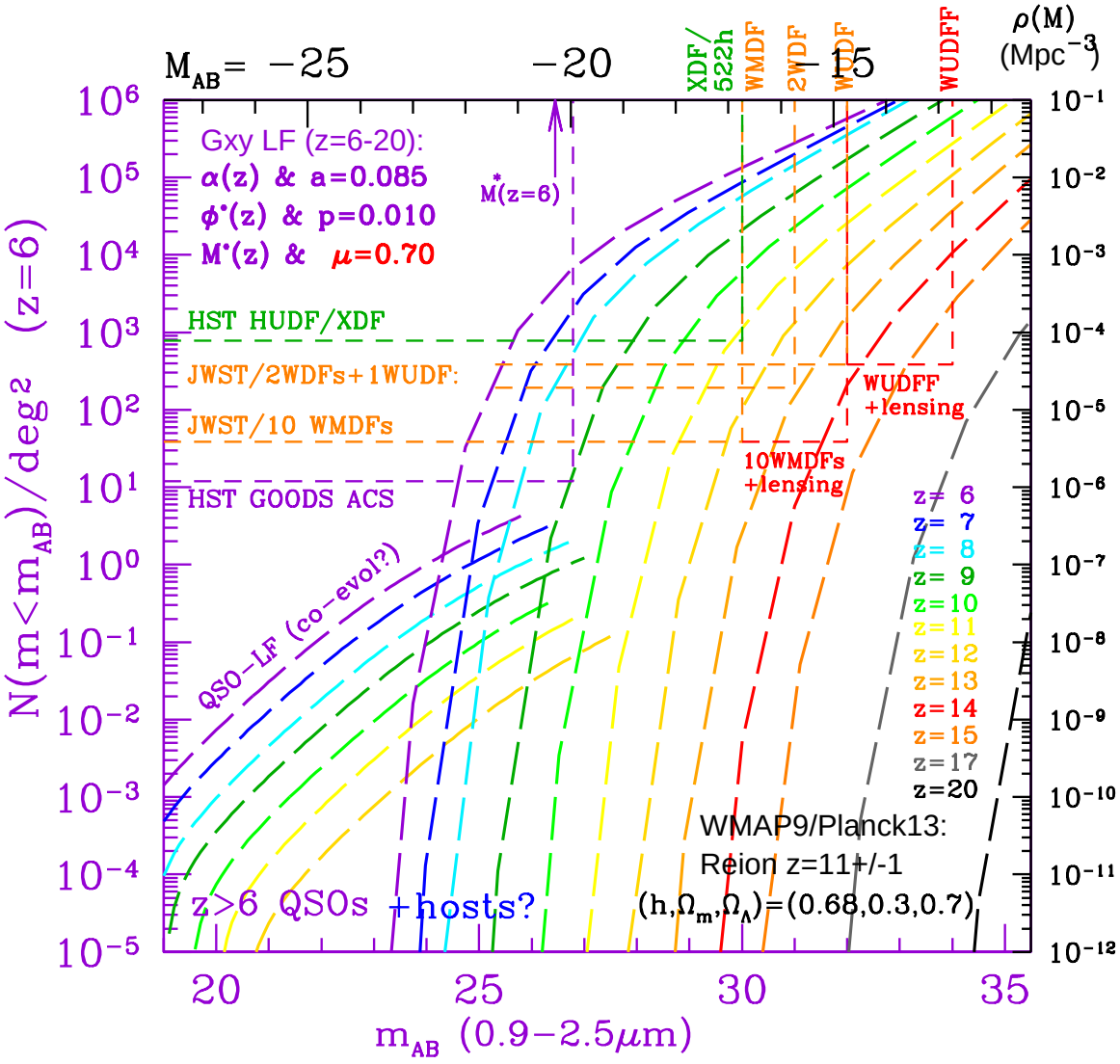

Fig. 7a: Schechter prediction of the galaxy LF for z$\lesssim$6$\lesssim$20 using α(z), Φ^* (z), and M^* (z) from Fig. 4abc. The possible redshift evolution of these Schechter parameters is captured by the 3 indicated parameter values as discussed in §2.2, Eq. (3a)–(3g), and Fig. 4abc. The Schechter prescription gives predictions in *physical* units as a function of M_{AB} (in mags) and space density ρ(M) (in Mpc) as indicated by the black axes at the top and on the right, respectively. The corresponding *observed* quantities are m_{AB} and the number density N(m), respectively, and are indicated along the purple bottom and left axes, respectively. These curves are only exact for z=6 (purple), but we shifted the other colored curves to be approximately correct for z$\gtrsim$7 as well, using our adopted WMAP9/Planck13 cosmology. (As a consequence, the black M_{AB} and ρ(M) axes are only correct for z=6, and are shifted by $\sim$+0.78 mag and -0.3dex at z$\simeq$10) — this does not affect the current discussion in any major way). The HUDF/XDF field-of-view and detection limit are indicated by the horizontal and vertical lines respectively. Similar lines are shown for HST GOODS in purple and for the various JWST surveys in orange. The latter are: the Webb Medium Deep Survey (10 WMDF pointings), the Webb Deep Field (2 WDF pointings are assumed), and the Webb UltraDeep Field (1 WUDF pointing). For the 10 WMDF and 1 WUDF pointings, the red wedge indicates the gain obtained in sensitivity due to gravitational lensing, if these are pointed at foreground clusters or rich groups with significant compactness. The (lensed) Webb deep fields will likely be able to find "first light" objects to z$\lesssim$13 (to z$\lesssim$15–16 when lensed), but such objects may be quite rare if the HUDF is representative enough for above predictions.

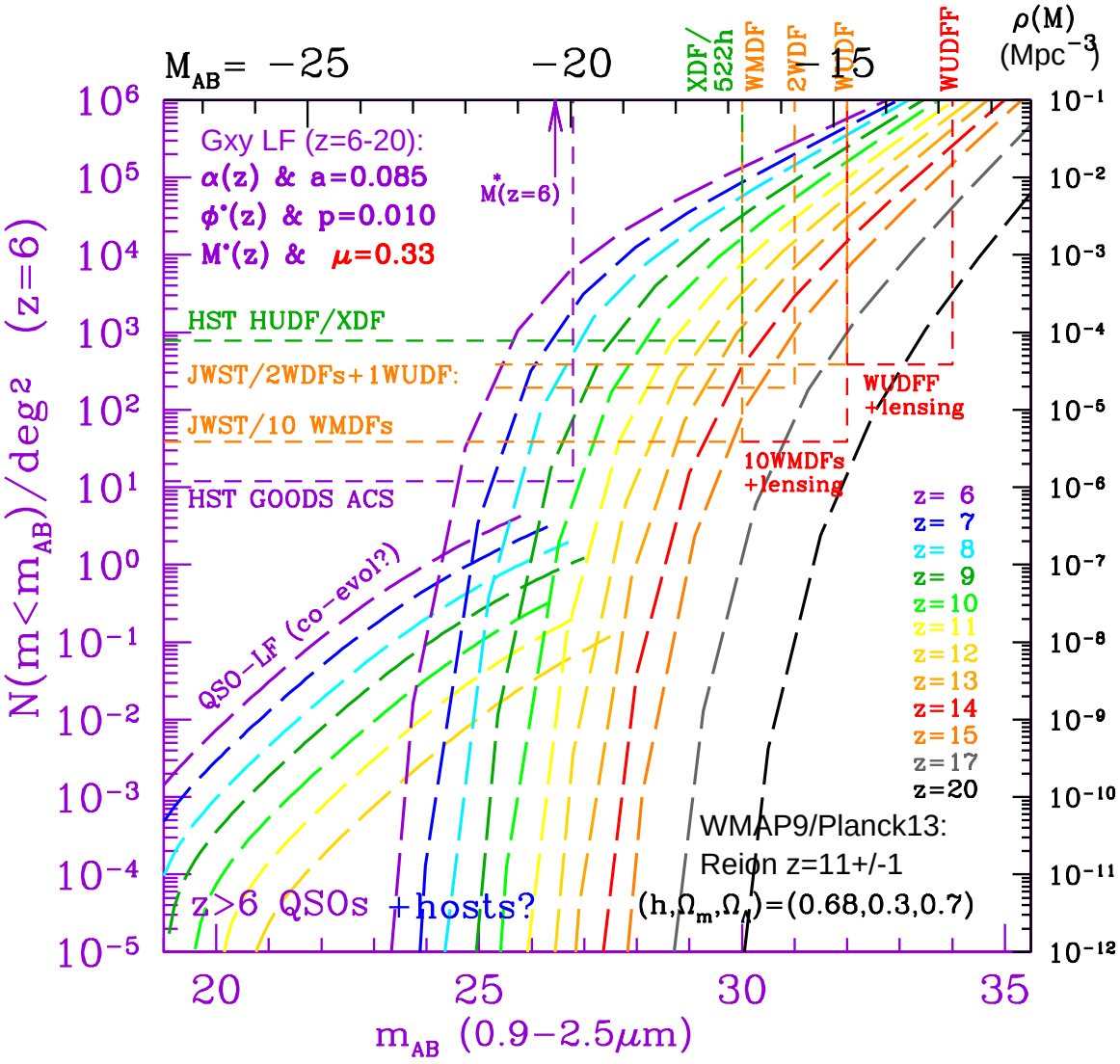

Fig. 7b: Same as Fig. 7a, but with the M^* (z) evolution parameter set to μ=0.33, as in Oesch et al. (2013). This shows that the M^* (z$\gtrsim$8) behavior in Fig. 4a cannot continue to decline with redshift as slowly as it does for 3.5$\lesssim$z$\lesssim$8, or far more objects at 9$\lesssim$z$\lesssim$12 would have been seen in the XDF, even though the number of objects at 6$\lesssim$z$\lesssim$8 remains roughly the same as in Fig. 7a. Instead, as we suggest in Fig. 4c, 5a, and 7b, M^* (z$\simeq$9) is likely fainter than –18.0$\pm$0.5 mag, while M^* (z$\simeq$11) may be fainter than –17.5$\pm$0.5 mag.

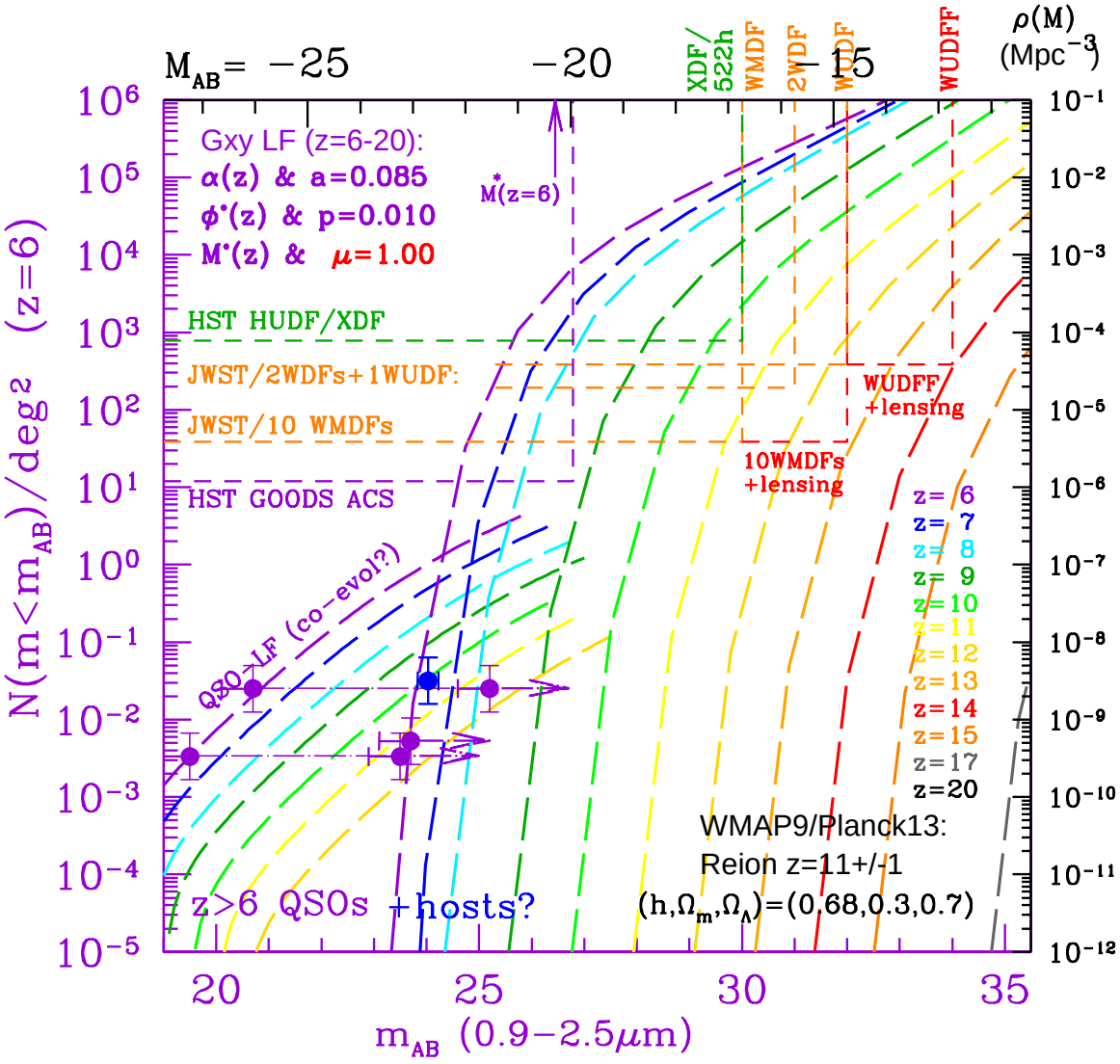

Fig. 7c: Same as Fig. 7b, but with the M^* (z) evolution parameter set to μ=1.00, which is still allowed by the data in Fig. 4c. Such large values of μ produce a significant decline in M^* for z$\gtrsim$8. As a consequence, the LF at z$\gtrsim$8 would drop dramatically and result in far fewer high redshift objects expected for JWST at z$\gtrsim$12–13. The only other data added here are the upper limits to the z$\simeq$6 quasar host galaxy fluxes by Mechtley et al. (2012, 2013). The blue dot indicates their one possible host galaxy detection (Mechtley et al. 2013). The epoch dependent LF of quasars was not done with the Schechter prescription, and is only intended to illustrate the possible co-evolution of supermassive blackholes in AGN and that of massive galaxies, which *was* computed one with the Schechter LF. The QSO LF at z=6 was normalized to the known surface density of SDSS and other z=6 quasar surveys (Jiang et al. 2008, 2009).

3 III. Using Group Lensing to Optimize JWST First Light Surveys

Authors: Robert L. Barone-Nugent, J. Stuart B. Wyithe, Rogier A. Windhorst, Seth H. Cohen, Rolf A. Jansen, Simon P. Driver, Aaron S. G. Robotham, Mehmet Alpaslan, Rebecca Lange, Andrew M. Hopkins, Michelle Cluver, & Iraklis Konstantopoulos

3.1 Introduction

Deep surveys of Galaxy Assembly in the field and in clusters — present and future: The Sloan Digital Sky Survey (York et al. 2000), the Hubble (Ultra) Deep Fields (Williams et al. 1996; Beckwith et al. 2006), and subsequent HST Legacy surveys (COSMOS, GEMS, GOODS, CANDELS, CLASH and soon also forthcoming the Hubble Frontiers Field (HFF) cluster deep survey) provide a wealth of data on the very near ($z \lesssim 0.1$) and distant ($z \gtrsim 1$) Universes (i.e., the most recent Gyr, and the first 7 Gyrs after the Big Bang). The HST galaxy surveys cover either very rich high-mass ($>5\times10^{14} M_{\odot}$) clusters (mainly for lensing studies; e.g., Fig. 1a), or deep blank sky pointings which predominantly probe the field environment (e.g., Fig. 4b), where the contiguous coverage is generally insufficient to ascertain halo mass. Over 50% of today's integrated stellar mass in galaxies resides in low to intermediate mass halos with masses in the range $\sim 3\times10^{12}$–$5\times10^{14} M_{\odot}$ (Eke et al. 2005), and only 2% in rich clusters with $M \gtrsim 5\times10^{14} M_{\odot}$. This strongly argues that galaxy groups need a more prominent focus in galaxy assembly studies.

The most compact among the groupings contained in such halos (compact groups, CGs; Hickson 1992) have centrally concentrated mass profiles, similar to clusters (Mendes de Oliveira & Giraud 1994). Therefore, while they are not at the upper end of the halo mass function, CGs make great lenses in three ways: (i) they vastly outnumber clusters and can therefore gravitationally amplify high-z galaxies above faint detection thresholds over greater areas; (ii) they feature much less intra-group light, which can be confused with lensed galaxy arcs; (iii) with fewer members they are simpler to model as lenses.

3.2 Finding the Optimum Lensing Sample for First Light Objects at $z \gtrsim 10$

Fig. 1a–1b illustrate the enormous drop in surface density between $z \simeq 7$–8 and $z \simeq 9$–12, which — if real — may indicate a significant drop in M^* at $z \gtrsim 8$ (Fig. 4c). If M^* indeed drops below $\gtrsim$–18 mag at $z \gtrsim 10$, this could trigger the need for gravitational lensing studies of the faint galaxy population at $z \gtrsim 10$ with JWST (e.g.,Wyithe et al. 2011; Barone-Nugent et al. 2013).

Targeting rich clusters *will* penetrate deeper into the galaxy LF, because their gravitational magnification will be larger, but may also reduce the number of $z \gtrsim 9$–12 objects that enter the deep field samples *unlensed*, because they are harder to see between the many foreground cluster objects, and due to the extended cluster halo-light (Fig. 1a).

In the current study, we therefore propose to complement existing HST and HFF cluster lensing work with group-lensing studies, since in galaxy groups it may be easier to separate and remove JWST straylight gradients, and groups may provide better $A\times\Omega$ than rich clusters for lensing work at $z \gtrsim 10$. Our goal of this study is to identify and prepare a significant number of massive galaxy groups at $0.3 \lesssim z \lesssim 0.45$, which have less intra-cluster light. They will provide significant lensing

magnification and will cover much more area both with HST BVi and JWST 1–10μm images to measure the brighter-end of the galaxy LF at $z \gtrsim 10$ (Fig. 7abc).

3.3 Available Galaxy Groups from the GAMA Survey at $z \lesssim 0.45$.

Here we discuss the use of the panchromatic GAMA database to identify massive galaxy groups at $0.02 \lesssim z \lesssim 0.45$: The GAMA survey (Baldry et al. 2010; Driver et al. 2011) samples five 60-sq deg regions to $r \lesssim 19.8$ mag (i.e., 2 mag deeper than SDSS main), and spectroscopically samples each region multiple times (typically $7\times$), which enables galaxy pairs, triplets, and groups to be fully measured. Panchromatic GAMA data is provided by GALEX MIS (UV); VST KIDS (optical); VISTA VIKING (near-IR); WISE (mid-IR), Herschel-Atlas (far-IR); ASKAP-DINGO (20cm, 21cm), and GMRT (1m and 3m), with sub-regions covered by CFHT-Lens and XMM-XXL. The GAMA survey yielded 360,000 galaxies with spectroscopic redshifts to $r \lesssim 19.8$ mag at the 4 m AAO telescope, and 36 million galaxies with 20-band GAMA photometric redshifts to $r \lesssim 24$ mag, based on VST & VISTA observations that are being completed in 2013.

The GAMA galaxy group catalog (Robotham et al. 2011) was constructed from the spectroscopic galaxy survey (Driver et al. 2011), using a modified friend-of-friends algorithm, and is shown here in Fig. 8. The 2013 GAMA catalog contains 22,442 galaxy groups, of which 2433 are robust with 5 or more spectroscopic members at $0.05 \lesssim z \lesssim 0.4$ (Fig. 8 here; see also Robotham et al. 2011).

The GAMA group catalog is, therefore, uniquely placed to sample the full range of group halo masses over the last 4 Gyr of cosmic time, and identify the best groups available at $0.3 \lesssim z \lesssim 0.45$ for JWST lensing studies at $z \gtrsim 10$–20, and in fact for the whole faint galaxy population at $z \gtrsim 3$.

3.4 Massive GAMA groups at $0.3 \lesssim z \lesssim 0.45$ as possible lensers of objects at $3 \lesssim z \lesssim 20$.

Given the arguments made in §II, it will be important that before JWST's launch in 2018 we identify a sufficiently large number of galaxy groups with significant lensing amplification — and with potentially lower predicted JWST straylight levels — that can be used for gravitational lensed "first light" studies at $z \gtrsim 10$–20, especially the bright-end of the First-Light LF (Fig. 2b–3).

We have selected the best and most compact GAMA groups at $0.3 \lesssim z \lesssim 0.45$ for JWST lensing studies at $z \lesssim 3$–20 (Fig. 8–10), that complement Hubble's three HUDF fields and 6 Cluster Frontier Fields. With a sample of $\sim 2\times10^5$ galaxies, the Galaxy and Mass Assembly survey (GAMA, Driver et al. 2003; Fig. 8) has mapped 200 sq. deg. of the equatorial sky, spectroscopically covering systems at $R \lesssim 20$ AB-mag. Approximately 40% of all GAMA galaxies are associated with a group, and of those we have isolated a sample of 8 compact groups at $z \simeq 0.35 \pm 0.05$ with masses between $M \simeq 10^{14}$–$10^{15} M_{\odot}$ and concentration profiles suitable for lensing galaxies at $2 \lesssim z \lesssim 20$, *i.e.*, $\lesssim 2$ Gyr after the Big Bang. From the GAMA group sample of 22,000 groups, 2400 have $\gtrsim 5$ spectroscopic redshifts that indicate gravitationally bound groups. From these, we selected the groups most appropriate for high redshift lensing as follows. In brief, we derived the concentration of all GAMA groups at $z \simeq 0.35 \pm 0.05$ via the group dynamical mass, and from that we derived the slope between the 50th and 68th percentile radii. We then applied theoretical and observational expectations of the dark matter halo in which the GAMA compact groups are embedded and the luminosity function

of the target high-z galaxy population (see §II), to estimate the number of lensed systems that can be detected to AB$\lesssim$30–31 mag, as appropriate for JWST observations.

Fig. 9 shows the GAMA group mass versus concentration and the number of expected lensed sources (as numbered contours), assuming an Navarro Frenk, & White (1996) dark matter halo mass profiles. The GAMA survey has 22,000 groups, more than 2400 of which have N$\gtrsim$5 spectroscopic redshifts. From these, we we propose to observe the best, most concentrated GAMA groups to optimize the chance of seeing objects in the epoch of reionization and first light through lensing studies at z$\gtrsim$6–15.

The lensing probabilities were calculated as in Barone-Nugent et al. (2013), with contours indicating the number of lensed objects behind each GAMA group of given redshift, mass, and concentration. GAMA group concentrations are estimated through the 50th and 68th percentile radii of enclosed mass. The model of the expected lensed galaxies assumes an AB-limit $\lesssim$30 mag (4×2 hrs for the JWST WMDF), and the observed α(z), Φ^* (z) and M^* (z) relations of Fig. 4abc, as extrapolated for z$\gtrsim$10. The total number of lenses expected in the redshifts ranges of 2$\lesssim$z$\lesssim$15 and 6$\lesssim$z$\lesssim$15 (dashed full-drawn lines, respectively) are summed-up for all lensed objects expected for each GAMA group using redshift slices with width of Δz=1. Medium-deep JWST images (WMDF) on the 10 GAMA groups best suited for lensing will add $\sim$50–100 lensed galaxies to AB$\lesssim$30 mag at z$\simeq$6–15, and $\gtrsim$10× more (or $\gtrsim$500) lensed sources at $\simeq$2–15. To AB$\lesssim$32 mag, the WUDFF — if pointed at a lensing massive group or cluster — would add another 6× more, or potentially $\gtrsim$3000 lensed sources at 6$\lesssim$z$\lesssim$15, respectively. At this flux level, the JWST images will be so crowded that a new generation object-finding algorithms may be needed — that fully remove all foreground objects (see §I) — to get complete samples of the lensed sources at z$\gtrsim$6–15.

3.5 Future Work on the GAMA samples: New Data and Modeling needed.

• (4a) We are proposing to obtain and will reduce/analyze/publish additional BVi images of GAMA groups during HST's remaining life-time **(led by Driver and his group at ICRAR and Windhorst's group at ASU.** This part is paid for by HST grants, not JWST funds.

• (4b) We will also propose to get deeper AAT and Gemini GAMA group galaxy-spectra for z$\lesssim$0.45 and R$\lesssim$24 mag. Write proposals and obtain/reduce/analyze/publish data. This is in collaboration with Hopkins and his group at AAO and Driver and his group at ICRAR.

• (4c) Make weak-lensing shear-maps for the best available GAMA groups at 0.3$\lesssim$z$\lesssim$0.45, using the available HST images and panchromatic 20-band GAMA z_{phots}'s for AB$\lesssim$24 objects **(led by Wyithe and Barone-Nugent at U. Melbourne).**

Analytical calculation of the lensing cross section — assuming a point mass for the group — approximates it as $\pi\ \theta_E^2$, where the Einstein Radius θ_E is given as a function of group lensing mass and source/lens angular size distances: θ_E = $(4GM/c^2\ \times\ D_{ds}/D_d/D_s)^{\ 0.5}$ and suggests that for faint JWST objects at z$\simeq$3–15, a compact GAMA group at z$\simeq$0.4 with mass M$\simeq$$10^{15} M_\odot$(Fig. 8b) has a lensing cross section that is $\sim$16×larger than a COSMOS group at z$\simeq$0.75 with mass M$\simeq$$10^{14} M_\odot$.

We will need to do the full numerical calculation with the actual GAMA group velocity dispersions and their actual sizes, which are given in, or implicit in Fig. 10. We will do the same for the COSMOS sample, as it may yield additional suitable compact group lenses at z$\gtrsim$0.5.

Other questions to address are as follows. For optimal lensing of z$\simeq$3–20 objects, does a GAMA group at z$\simeq$0.3–0.4:

i) Need to have an N(z) that is Gaussian, or does the group need to be virialized in σ_v? This will be addressed from studies like Fig. 9–10.

ii) Need to be very compact? How compact in parameters Rad50, Rad1Sig, or Rad100?

iii) Need to be spherical or elliptical in the sky?

iv) What is the optimum mix of area and depth to optimally sample cosmic variance in "first light" studies at z$\gtrsim$10?

• (4d) Prepare the appropriate GAMA groups as targets for JWST GTO time.

Acknowledgements: This work was supported by NASA JWST Interdisciplinary Scientist grant NAG5-12460 from NASA Goddard Space Flight Center.

References:

Alpaslan, M., et al. 2012, MNRAS, 426, 2832
Baldry I.K., et al. 2010, MNRAS, 404, 86
Baldry I., et al. 2012, MNRAS, 421, 621
Barone-Nugent, R. L., Wyithe, J. S. B., et al. 2013, MNRAS, submitted
Bouwens, R. J., et al. 2007, ApJ, 670, 928
Bouwens, R. J., et al. 2011b, ApJ,737,90
Bowers, C. et al. 2013, Presentation to the JWST Science Working Group
Driver S.P., Robotham A.S.G., 2010, MNRAS, 407, 2131
Driver S.P., & Robotham A., et al. 2011, MNRAS, 413, 2570
Driver S.P., et al. 2012, MNRAS, 427, 3244
Driver S.P., et al. 2013, MNRAS, in press (arXiv:1301.979)
Eke V., et al. 2005, MNRAS, 362, 1233
http://www.gama-survey.org
Gardner, J. P. 1998, PASP, 110, 291
Jansen, R. A., Collins, N., & Windhorst, R. A. 2003, in "The 2002 HST Calibration Workshop: Hubble After the Installation of the ACS and the NICMOS Cooling System", Eds. S. Arribas, A. Koekemoer, & B. Whitmore, (STScI: Baltimore), p. 193
Jansen, R. A., Windhorst, R., Kim, H., Hathi, N., Goudfrooij, P., & Collins, N. 2010, in Proc. of the "2010 HST Calibration Workshop", Eds. S. Deustea & C. Oliveira (Baltimore: STScI), pg. 455–461
Khochfar, S., et al. 2013, astro-ph/1311.xxxx
Knobel, C. Lilly, S. J., et al. 2012, ApJ, 753, 121
Oesch, P. A., et al. 2013, ApJ, 773, 75
Robotham A., et al. 2010, PASA, 27, 76
Robotham A., et al. 2011, MNRAS, 416, 2640
Robotham A., et al. 2012, MNRAS, 424, 1448
Robotham A., et al. 2013, MNRAS, in press (arXiv:1301.7129)
Somerville, R. S. et al. 2004, ApJ, 600, L171
Williams R., et al. 1996, AJ, 112, 1335
York D., et al. 2000, AJ, 120, 1579
Windhorst, R. A., et al. 2011, ApJS, 193, 27
Windhorst, R. A. 2012, Internal Technical Report to the JWST Project:

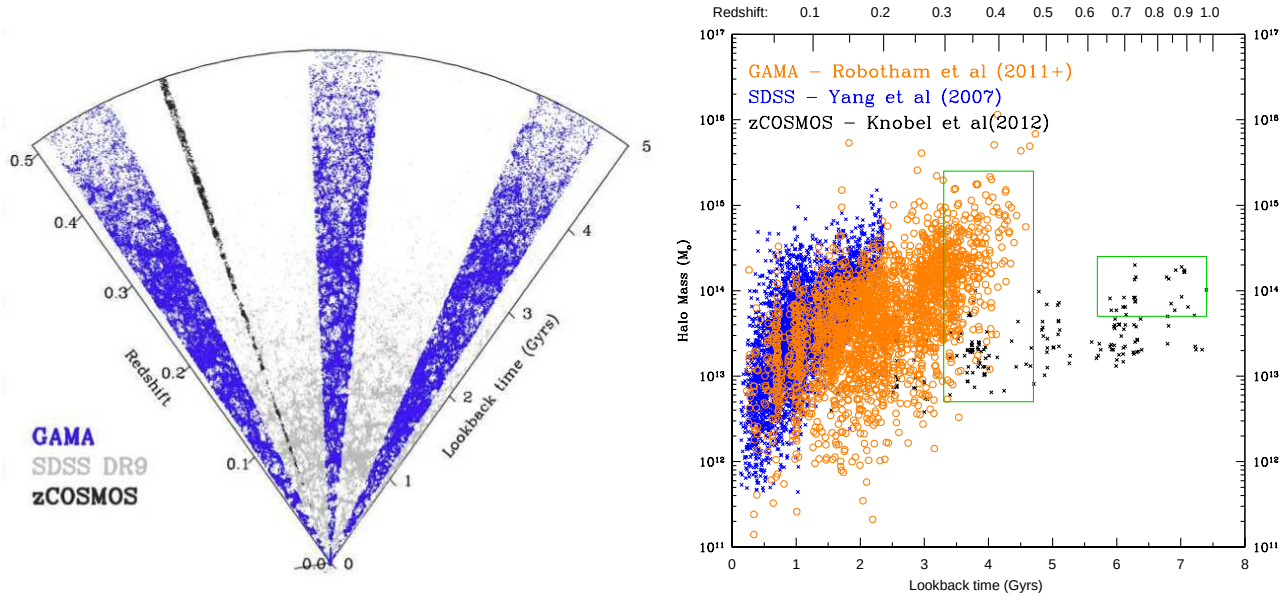

Fig. 8:

(*Fig. 8a; left*): Cone diagrams showing the galaxy distribution of GAMA, the SDSS DR9 and the zCOSMOS data sets, respectively. GAMA offers a prime galaxy group and galaxy survey in the redshift range $0.1 \lesssim z \lesssim 0.4$, which covers the last 4 billion years, and uniquely samples the gap between SDSS ($z \lesssim 0.1$) and zCOSMOS ($z \gtrsim 0.4$), and also provides multiple lines of sight to minimize cosmic variance.

(*Fig. 8b; right*): Comparison of SDSS groups at $z \lesssim 0.25$ (Yang et al. 2007), GAMA groups at $z \lesssim 0.45$ (Robotham et al. 2011), and COSMOS groups at $z \lesssim 1.0$ (Knobel et al. 2012). While COSMOS group reach to $\sim 2\times$ larger redshifts, GAMA groups reach larger masses due to GAMA's much larger survey volume. Since $\lesssim 10\%$ of high-multiplicity (N<4) groups are compact (Konstantopoulos et al. 2013), GAMA's large group sample is required to identify optimal candidate lenses. For faint JWST objects at $z \simeq 3$–15, a compact GAMA group at $z \simeq 0.4$ with mass $M \simeq 10^{15} M_{\odot}$(Fig. 8a) has a lensing cross section $\sim 16\times$larger than a COSMOS group at $z \simeq 0.75$ with mass $M \simeq 10^{14} M_{\odot}$ (for details, see text).

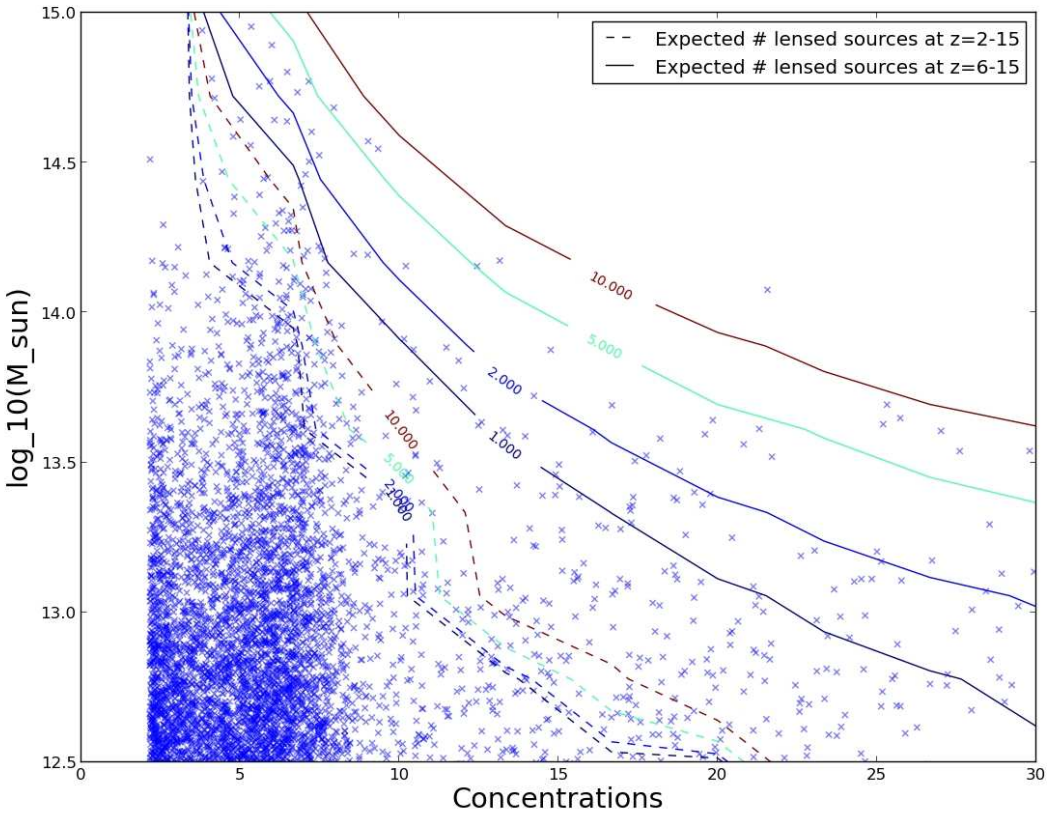

(*Fig. 9*): GAMA group mass versus concentration and the number of expected lensed sources (as numbered contours), assuming an Navarro Frenk, & White (1996) dark matter halo mass profiles. The GAMA survey has 22,000 groups, more than 2400 of which have N$\gtrsim$5 spectroscopic redshifts. From these, we propose to observe the best, most concentrated GAMA groups to optimize the chance of seeing objects in the epoch of reionization and first light through lensing studies at z$\gtrsim$6–15. The lensing probabilities were calculated as in Barone-Nugent et al. (2013), with contours indicating the number of lensed objects behind each GAMA group of given redshift, mass, and concentration. GAMA group concentrations are estimated through the 50th and 68th percentile radii of enclosed mass. The model of the expected lensed galaxies assumes an AB-limit $\lesssim$30 mag (4$\times$2 hrs for the JWST WMDF), and the observed α(z), Φ^* (z) and M^* (z) relations of Fig. 4abc, as extrapolated for z$\gtrsim$10. The total number of lenses expected in the redshifts ranges of 2$\lesssim$z$\lesssim$15 and 6$\lesssim$z$\lesssim$15 (dashed full-drawn lines, respectively) are summed-up for all lensed objects expected for each GAMA group using redshift slices with width of Δz=1. Medium-deep JWST images (WMDF) on the 10 GAMA groups best suited for lensing will add $\sim$50–100 lensed galaxies to AB$\lesssim$30 mag at z$\simeq$6–15, and $\gtrsim$10$\times$ more (or $\gtrsim$500) lensed sources at $\simeq$2–15. To AB$\lesssim$32 mag, the 800 hr WUDFF — if pointed at a lensing massive group or cluster — would add another $\sim$6$\times$ more, or potentially $\gtrsim$3000 lensed sources at 6$\lesssim$z$\lesssim$15, respectively. At this flux level, the JWST images will be so crowded that a new generation object-finding algorithms may be needed — that fully remove all foreground objects (see §I) — to get complete samples of the lensed sources at z$\gtrsim$6–15.

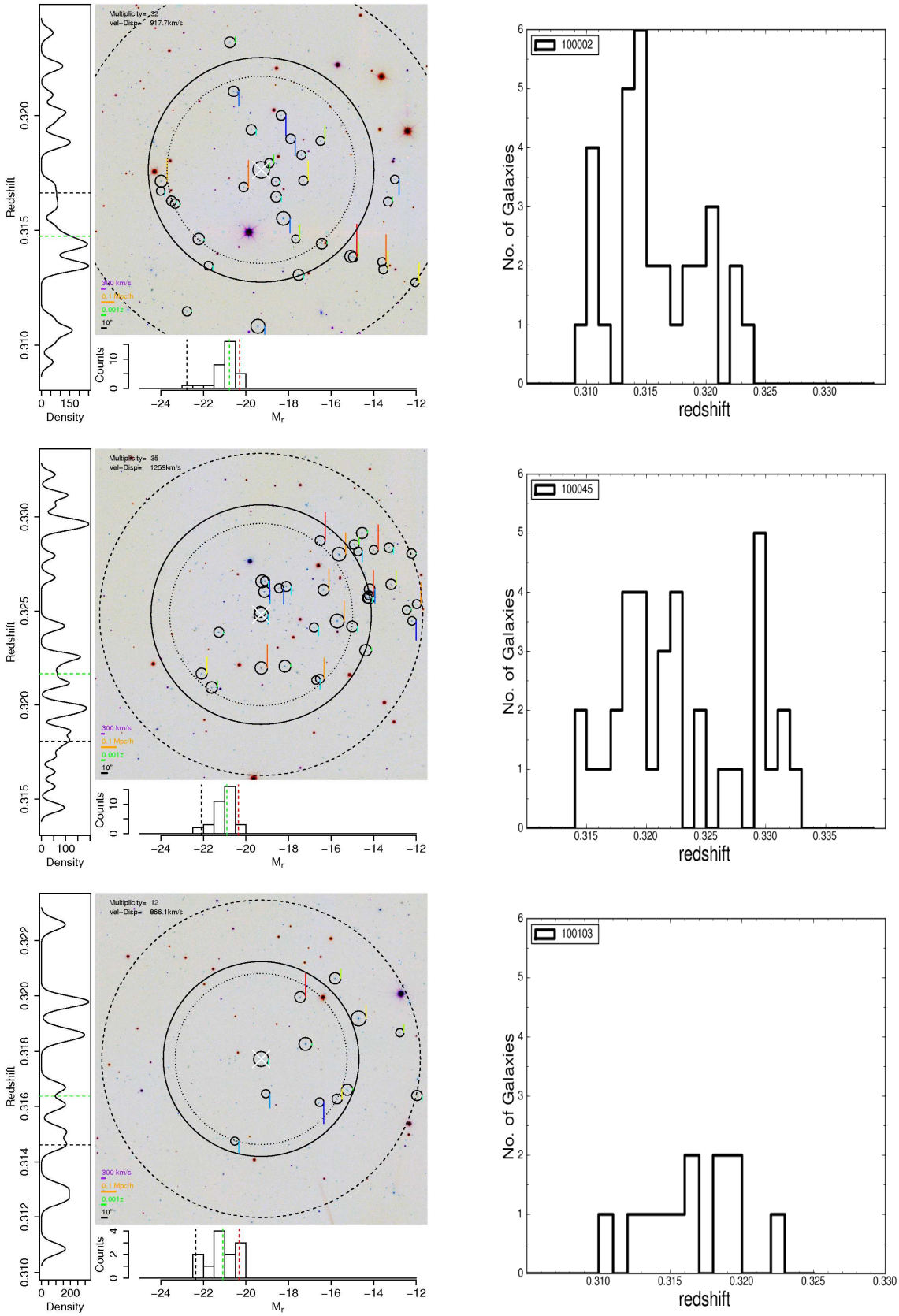

Fig. 10: (*10a; left panels*): GAMA group finding chart from SDSS with members having secure AAT redshifts indicated for R $\lesssim$ 19.8 AB-mag, as well as the redshift probability distribution and absolute magnitude (ML_r) distribution. (*10b; right panels*): Measured GAMA group redshift distribution for GAMA group numbers: 100002g09, 100045g09, and 100103g09.

3. NAME AND (ANTICIPATED) DATE OF PUBLICATIONS RELEVANT TO JWST:

Below we list papers that are based (in part) on results from this JWST grant, and that have implications for the science requirements and survey planning of JWST. Papers that only publish HST data are funded separately by STScI. [Not all papers listed below that are relevant to JWST's performance are discussed in detail above.]

PDF files of all papers published and presentations given during this FY are available upon request. Most are also available on the following website:
www.asu.edu/clas/hst/www/jwst/ and adsabs.harvard.edu/abstract_service.html

3a. REFEREED PAPERS IN PRINT/PRESS RELEVANT FOR JWST SCIENCE:

"Triggered Star-formation in the Inner Filament of Centaurus A"
Crockett, R. M., Shabala, S. S., Kaviraj, S., Antonuccio-Delogu, V. Silk, J., Mutchler, M., O'Connell, R. W., Rejkuba, M., Whitmore, B. C., & Windhorst, R. A. 2012, MNRAS, 421, 1603–1623 (21 pp) (astro-ph/1201.3369)

"A Panchromatic Catalog of Early-Type Galaxies at intermediate redshift in the Hubble Space Telescope Wide Field Camera 3 Field"
Rutkowski, M. J., Cohen, S. H., Windhorst, R. A., O'Connell, R. W., Crockett, M., Kaviraj, S., Silk, J., Kimble, R., Balick, B., Bond, H. E., Calzetti, D., Disney, M. J., Dopita, M. A., Frogel, J. A., B. Hall, D. N., Holtzman, J. A., Kimble, R. A., Luppino, G., McCarthy, P. J., Paresce, F., Saha, A., Trauger, J. T., Walker, A. R., Whitmore, B. C., & Young, E. T. 2012, ApJS, 199, 4 (20 pp) (astro-ph/1201.6416)

"The Size Evolution of Passive Galaxies: Observations from the Wide Field Camera 3 Early Release Science Program"
Ryan, R. E. Jr., McCarthy, P. J., Cohen, S. H., Yan, H., Hathi, N. P., Koekemoer, A. M., Rutkowski, M. J., Mechtley, M. R., Windhorst, R. A., O'Connell, R. W., Balick, B., Bond, H. E., Bushouse, H., Calzetti, D., Crockett, R. M., Disney, M., Dopita, M. A., Frogel, J. A., Hall, D. N. B., Holtzman, J. A., Kaviraj, S., Kimble, R. A., MacKenty, J., Mutchler, M., Paresce, F., Saha, A., Silk, J. I., Trauger, J., Walker, A. R., Whitmore, B. C., & Young E. 2012, ApJ, 749, 53 (11 pp) (astro-ph/1007.1460)

"A WFC3 Study of Globular Clusters in NGC 4150: An Early-Type Minor Merger"
Kaviraj, S., Crockett, R. M., Whitmore, B. C., Silk, J., O'Connell, R. W., Windhorst, R. A., Mutchler, M., Rejkuba, M., Yi, S., Frogel, J. A., & Crockett,2012, MNRAS, 422, L96–100 (5 pp) (astro-ph/1107.5042)

"Population Study of Resolved Stars in M83 using HST/WFC3 Early Release Science Data"
Kim, H., Whitmore, B. C., Chandar, R., Saha, A., Windhorst, R. A., Balick, B., Bond, H. E., Calzetti, D., Carollo, C. M., Disney, M. J., Dopita, M. A., Frogel, J. A., Hall, D. N. B., Holtzman, J. A., Kimble, R. A., Luppino, G., McCarthy, P. J., O'Connell, R. W., Paresce, F., , Silk, J. I., Trauger, J. T., Walker, A. R., & Young, E. T. 2012, ApJ, 753, 26 (22 pp) (astro-ph/1204.6045)

"Metallicities of Emission-Line Galaxies from HST ACS PEARS and HST WFC3 ERS Grism Spectroscopy at $0.6<z<2.4$"
Xia, L., Malhotra, S., Rhoads, J., Pirzkal, N., Straughn, A., Finkelstein, S., Cohen, S., Kuntschner, H., Kümmel, M., Walsh, J., Windhorst, R. A., & O'Connell, R. 2012, AJ, 144, 28 (11 pp) (astro-ph/1205.3172)

"The Road to the Red Sequence: A Detailed View of the Formation Massive Galaxy at $z\sim2$."
Ferreras, I., Pasquali, A., Khochfar, S., Kuntschner, H., Kuümmel, M., Pirzkal, N., Windhorst, R., Malhotra, S., Rhoads, J., & O'Connell, R. W., Cohen, S., Hathi, N. P., Ryan, R. E. Jr., & Yan, H., 2012, AJ, 144, 47 (11 pp) (astro-ph/1109.6323)

"Infrared Imaging of a z=6.42 Quasar Host Galaxy with the Hubble Space Telescope Wide Field Camera 3"

Mechtley, M., Windhorst, R. A., Ryan, R. E., Schneider, G., Cohen, S. H., Jansen, R. A., Fan, X., Hathi, N. P., Keel, W. C., Koekemoer, A. M., Röttgering, H., Scannapieco, E., Schneider, D. P., Strauss, M. A., & Yan, H. J. 2012, ApJL, 756, L38 (4 pp) (astro-ph/1207.3283)

"Constraining Stellar Assembly and Active Galactic Nucleus Feedback at the Peak Epoch of Star-Formation"
Kimm, T., Kaviraj, S., Devriendt, J. E. G., Cohen, S. H., Windhorst, R. A., Dubois, Y., Slyz, A., Hathi, N. P., Ryan, R. E. Jr., O'Connell, R. W., Dopita, M. A., & Silk, J. 2012, MNRAS, 425, L96–L100 (5 pp) (astro-ph/1205.3801)

"Newborn Spheroids at High Redshift: When and How did the Dominant, Old Stars in Today's Massive Galaxies Form?"
Kaviraj, S., Cohen, S., Ellis, R. S., Peirani, S., Windhorst, R. A., O'Connell, R. W., Silk, J., Whitmore, B. C., Hathi, N. P., Ryan, R. E. Jr., Dopita, M. A., Frogel, J. A., & Dekel, A. 2013, MNRAS, 428, 925–934 (10 pp) (astro-ph/1206.2360)

"The Insignificance of Major Mergers in Driving Star-Formation at $z \simeq 2$"
Kaviraj, S., Cohen, S. H., Windhorst, R. A., Silk, J., O'Connell, R. W., Dopita, M. A., Dekel, A., Hathi, N. P., Straughn, A., & Rutkowski, M. 2013, MNRAS, 429, L40–L44 (5 pp) (astro-ph/1210.4160)

"Stellar Populations of Lyman Break Galaxies at $z \simeq 1$–3 in the HST/WFC3 Early Release Science Observations"
Hathi, N. P., Cohen, S. H., Ryan, R. E. Jr., Finkelstein, S. L., McCarthy, P. J., Windhorst, R. A., Yan, H., Koekemoer, A. M., Rutkowski, M. J., O'Connell, R. W., Straughn, A. N., Balick, B., Bond, H. E., Calzetti, D., Disney, M. J., Dopita, M. A., Frogel, J. A., Hall, D. N. B., Holtzman, J. A., Kimble, R. A., Paresce, F., Saha, A., Silk, J. I., Trauger, J. T., Walker, A. R., Whitmore, B. C., & Young, E. T. 2013, ApJ, 765, 88 (10 pp) (astro-ph/1206.6116)

"Investigating the Core Morphology–Seyfert Class relationship with Hubble Space Telescope Archival Imaging of local Seyfert galaxies"
Rutkowski, M, J., Hegel, P. H., Kim, H., Tamura, K., & Windhorst, R. A. 2013, AJ, 146, 11 (21 pp) (astro-ph/1301.4621)

"Emission-Line Galaxies from the Hubble Space Telescope Probing Evolution and Reionization Spectroscopically (PEARS) Grism Survey. II: The Complete Sample"
Pirzkal, N., Rothberg, B., Ly, C., Malhotra, S., Rhoads, J. E., Grogin, N. A., Dahlen, T., Meurer, G. R., Walsh, J. R., Hathi, N. P., Cohen, S. H., Bellini, A., Holwerda, B. W., Straughn, A. N., Mechtley, M. & Windhorst, R. A. 2013, ApJS, 772, 48 (17 pp) (astro-ph/1208.5535)

"Physical Properties of Spectroscopically-Confirmed Galaxies at $z \gtrsim 6$. I. Basic Characteristics from Deep HST and Spitzer Observations"
Jiang, L., Egami, E., Mechtley, M., Fan, X., Cohen, S. H., Windhorst, R. A., Davé, R., Finlator, K., Kashikawa, N., Ouchi, M., & Shimasaku, K. 2013, ApJ, 772, 99 (20 pp) (astro-ph/1303.0024)

"A Lyman Break Galaxy in the Epoch of Reionization from HST Grism Spectroscopy"
Rhoads, J. E., Malhotra, S., Stern, D., Dickinson, M., Pirzkal, N., Spinrad, H., Reddy, N., Hathi, N., Grogin, N., Koekemoer, A., Peth, M. A., Cohen, S., Zheng, Z., Budavari, T., Ferreras, I., Gardner, J., Gronwall, C., Zoltan H., Meurer, G., Moustakas, L., Panagia, N., Pasquali, A., Sahu, K., di Serego Alighieri, S., Straughn, A., Somerville, R., Walsh, J., Windhorst, R., Xu, C., & Yan H. 2013, ApJ, 773, 32 (7 pp) (astro-ph/1302.7005)

"Physical Properties of Spectroscopically-Confirmed Galaxies at $z \gtrsim 6$. II. Morphology of the Rest-Frame UV Continuum and Lyman-alpha Emission"
Jiang, L., Egami, E., Fan, X., Windhorst, R. A., Cohen, S. H., Davé, R., Finlator, K., Kashikawa, N., Mechtley, M., Ouchi, M., & Shimasaku, K. 2013, ApJ, 773, 153 (14 pp) (astro-ph/1303.0027)

3b. PAPERS SUBMITTED/IN PREPARATION RELEVANT TO JWST:

(see our report on these next year):

"Early-Type Galaxies at Intermediate Redshift Observed with HST WFC3: New Perspectives on Residual Star-Formation"
Rutkowski, M. J., Jeong, H., Cohen, S. H., Kaviraj, S., Yi, S., O'Connell, R. W., Hathi, N. P. Windhorst, R. A., Ryan Jr., R. E., Crockett, M., Yan, H., Kimble, R., Silk, J., McCarthy, P. J., Koekemoer, A. Balick, B., Bond, H. E., Calzetti, D., Disney, M. J., Dopita, M. A., Frogel, J. A., B. Hall, D. N., Holtzman, J. A., Paresce, F., Saha, A., Trauger, J. T., Walker, A. R., Whitmore, B. C., & Young, E. T. 2013, ApJ, in preparation

"Methods for Creating and Evaluating 3D Tactile Images to Teach STEM Courses to Visually Impaired and Blind Students"
Hasper, E., Windhorst, R. A., Baluch, D. P., Hedgpeth, H., Harris, L., Gonzales, A., Yu, H. & Farkas, Z. 2013, J. of Science Teacher Education, submitted (astro-ph/1304.xxxx)

"A WFPC2 Archival Study to Map the All-Sky Zodiacal Background: Constraints to the Faint Kuiper Belt Object population"
Windhorst, R. A., Jansen, R. A., Aloi, A., Bruursema, J., Cohen, S. H., Hutchison, H., Rogers, J., Kenyon, S., Gomez, M., & Petro, L. 2013, AJ, in preparation

"The Size Scale of Stellar Groupings in M83: from Compact Clusters to Stellar Complexes"
Kaleida, C. C., Whitmore, B. C., Chandar, R., Kim, H., Calzetti, D., Windhorst, R. A., Balick, B., Bond, H. E., Calzetti, D., Carollo, M., Disney, M. J., Dopita, M. A., Frogel, J. A., Hall, D. N. B., Holtzman, J. A., Kimble, R. A., Luppino, G., McCarthy, P. J., O'Connell, R. W., Paresce, F., Saha, A., Silk, J. I., Trauger, J. T., Walker, A. R., Whitmore, B. C., Windhorst, R. A., & Young, E. T. 2013, ApJ, in preparation

"Galaxy Sizes in the WFC3 Early Release Science Field"
Ashcraft, T., Cohen, S., Windhorst, R., Balick, B., Bond, H. E., Calzetti, D., Disney, M. J., Dopita, M. A., Frogel, J. A., B. Hall, D. N., Holtzman, J. A., Kimble, R. A., Luppino, G., McCarthy, P. J., O'Connell, R. W., Paresce, F., Saha, A., Silk, J. I., Trauger, J. T., Walker, A. R., Whitmore, B. C., & Young, E. T. 2013, ApJ, in preparation

"Appreciating Hubble At Hyper-speed: An Interactive Cosmology Visualization Web-tool using the Hubble UltraDeep Field"
Mechtley, M., Windhorst, R. A., Cohen, S. H., & Will, L. M. Summers, F., Pirzkal, N., Ryan, R. E. Jr., Malhotra, S., & Rhoads, J. 2013, PASP, in preparation

"Multi-Color Pixel-Based Analysis of Nearby Late-Type galaxies"
Tamura, K., Cohen, S. H., Jansen, R. A., & Windhorst, R. A. 2013, ApJ, in preparation

"Ten-Band Photometric Study of Distant Galaxies in the WFC3 Early Release Data: Redshifts and Physical Properties"
Cohen, S. H., Ryan, R. E. Jr., Hathi, N. P., Windhorst, R. A., Koekemoer, A., Balick, B., Bond, H. E., Calzetti, D., Disney, M. J., Dopita, M. A., Frogel, J. A., B. Hall, D. N., Holtzman, J. A., Kimble, R. A., Luppino, G., McCarthy, P. J., O'Connell, R. W., Paresce, F., Saha, A., Silk, J. I., Trauger, J. T., Walker, A. R., Whitmore, B. C., & Young, E. T. 2013, ApJ, in preparation

3c. REVIEW PAPERS IN PRINT OR IN PRESS RELEVANT TO JWST:

"Observing Galaxy Assembly with the James Webb Space Telescope"
Windhorst, R. A., 2013, in Space Telescope Science Institute Newsletter, Vol. 30, Issue 2, pg. 31–34, Eds. R. A. Brown (https://blogs.stsci.edu/newsletter/volume-30-issue-02/ ; Baltimore: Space Telescope Science Institute)

3d. NON-REFEREED CONFERENCE PAPERS IN PRINT/PRESS RELEVANT TO JWST:

"Active Galactic Nuclei and their role in Galaxy Formation and Evolution"

Kraemer, S., Windhorst, R., Carpenter, K. G., Crenshaw, M., Elvis, M., & Karovska, M. 2012, Science white paper submitted in response to the 2012 NASA COR RFI NNH12ZDA008L: "Science Objectives and Requirements for the Next NASA UV/Visible Astrophysics Mission", p. 1–8

"Galaxy Assembly and SMBH/AGN-growth from Cosmic Dawn to the End of Reionization"
Scowen, P., Jansen, R. A., Windhorst, R., Rhoads, J., Malhotra, S., Stern, D., O'Connell, R., Beasley, M., & the HORUS & SFC Science Concept Teams 2012, Science white paper submitted in response to the 2012 NASA COR RFI NNH12ZDA008L: "Science Objectives and Requirements for the Next NASA UV/Visible Astrophysics Mission", p. 1–7

"Minor-Merger-Driven Growth of Early-Type Galaxies over the Last 8 Billion Years"
Kaviraj, S., Crockett, R. M., Silk, J., Ellis, R. S., Yi, S. K., O'Connell, R. W., Windhorst, R., & Whitmore, B. C. 2012, in "The Spectral Energy Distribution of Galaxies", Eds. R. J. Tuffs & C. C. Popescu, IAU Symp. No. 284, 460–464 (International Astronomical Union)

" How Will Out-of-Field Straylight & Gravitational Lensing Bias Affect (Ultra-)Deep JWST Surveys and their Planning?"
Windhorst, R. A. 2012, Internal Technical Report to the JWST Project, (www.jwst.nasa.gov), p. 1–13

"Abell 1882: Kpc-scale Spatially Resolved Star formation on a z=0.14 "Proto-cluster""
Morrison, G. E., Sengupta, A., Keel, W. C., Windhorst, R. A., Smith, B., Owen, F. N., Dickinson, M. E., Arnouts S., Yun, M. S., Miller, N., & Drissen, L. 2013, in "Science with SITELLE", Wendake Workshop, Quebec

3e. NON-REFEREED ABSTRACTS IN PRINT/PRESS RELEVANT TO JWST:

"Probing Minor-merger-driven Star Formation in Early-type Galaxies using Spatially-resolved Spectro-photometric Studies"
Kaviraj, S., Crockett, M., Silk, J., O'Connell, R. W., Whitmore, B., Windhorst, R., Cappellari, M., Bureau, M., & Davies, R. 2012, BAAS, 219 (Abstract 102.01)

"Very Luminous Galaxy Population at z$>$7 as Revealed by HIPPIES"
Yan, H., & the HIPPIES Collaboration (incl. R. A. Windhorst) 2012, BAAS, 219 (Abstract 129.04)

""Observing" Images of a Simulated Universe: the High Redshift Luminosity Function"
Morgan, R. J., Scannapieco, E., Windhorst, R. A., & Thacker, R. 2012, BAAS, 219 (Abstract 129.05)

"WFC3 Imaging of z=6 Quasars: Examining The Host Galaxies of AGN in the Early Universe"
Mechtley, M., Windhorst, R. A., Ryan, R. E., Cohen, S. H., Schneider, G., Fan, X., Hathi, N. P., Jansen, R. A., Keel, W. C., Koekemoer, A. M. Röttgering, H., Scannapieco, E., Schneider, D. P., Strauss, M. A., & Yan, H. 2012, BAAS, 219 (Abstract 243.17)

"The Evolution of Lyman Break Galaxies Between z=1.5 and z=5.0"
Hathi, N. P., McCarthy, P. J., Cohen, S. H., Ryan, R. E., Jr., Windhorst, R. A., Yan, H., Rutkowski, M. J., Koekemoer, A. M., O'Connell, R. W., & the WFC3 Scientific Oversight Committee 2012, BAAS, 219 (Abstract 246.25)

"Multi-component SED Fitting Of AGN Host Galaxies
Cohen, S. H., Ryan, R. E., Windhorst, R. A., Grogin, N. A., Hathi, N. P., Straughn, A. N., Mechtley, M. R., Koekemoer, A. M., O'Connell, R. W., & the WFC3 Scientific Oversight Committee 2012, BAAS, 219 (Abstract 423.04)

"Investigating The Core Morphology–Seyfert Class Relationship Using Archival Hubble Space Telescope Images Of Local Seyfert Galaxies"
Windhorst, R. A., Rutkowski, M. J., Hegel, P., Kim, H., Tamura, K., & Corbin, M. R. 2012, BAAS, 219 (Abstract 435.07)

"Galaxy Structure in the Ultraviolet: Case studies for Galaxy Evolution"

Mager, V., Conselice, C., Seibert, M., Gusbar, C., Windhorst, R., & Madore, B. 2012, BAAS, 219 (Abstract 441.17)

"A Picture Worth a Thousand Words"
Gonzales, A. N., Harris, L. M., Brubaker, R., Windhorst, R. A., & Baluch, D. P. 2012, Microscopy & Microanalysis 2012 Meeting, Microscopy Society of America, Phoenix, AZ (Abstract LB-6)

"Enabling Blind Students to Tactilely Visualize Image Data"
Gonzales, A. N., Harris, L. M., Brubaker, R., Windhorst, R. A., & Baluch, D. P. 2012, Society for Neuroscience, New Orleans Meeting (October 2012)

"New tools that enable blind students to tactilely visualize image data"
Gonzalez, A., Harris, L., Brubaker, R., Windhorst, R., and Baluch, D.P. 2012, American Society for Cell Biology, San Francisco Meeting (November 2012)

"The Mass-Metallicity Relation of Emission-Line Selected Galaxies from HST Slitless Spectroscopy"
Rhoads, J., Xia, L., Malhotra, S., Pirzkal, N., Straughn, A., Finkelstein, S., Cohen, S., Kuntschner, H., Kuemmel, M., Walsh, J., Windhorst, R. A., & O'Connell, R. 2012, BAAS, 220 (Abstract 336.07)

"Investigating HST/WFC3 Selected Lyman Break Galaxies at z=1–3"
Hathi, N. P., McCarthy, P. J., Cohen, S. H., Ryan, R. E., Windhorst, R. A., Yan, H., Rutkowski, M. J., Koekemoer, A. M., O'Connell, R. W., & the WFC3 SOC 2013, BAAS, 221 (Abstract 228.06)

"Mechanisms for Galaxy Transformation in the Complex Environment of Super-Group Abell 1882"
Sengupta, A., Keel, W. C., Morrison, G. E., Windhorst, R. A., & Smith, B. 2013, BAAS, 221 (Abstract 304.07)

"A Search for z$\simeq$0.5-1.1 Ly-α Blobs"
Hegel, P., Jansen, R., & Windhorst, R. A. 2013, BAAS, 221 (Abstract 147.19)

"Stellar Population Gradients of Intermediate Redshift Galaxies"
Kim, D., Cohen, S. H., Windhorst, R. A., & WFC3 Scientific Oversight Committee 2013, BAAS, 221 (Abstract 147.35)

"Mapping the Resolved Stellar Population of the Dwarf Starburst Galaxy NGC 4214"
Kim, H., Whitmore, B. C., Cohen, S. H., Chandar, R., Kaleida, C. C., Windhorst, R. A., & the WFC3 Scientific Oversight Committee 2013, BAAS, 221, (Abstract 250.07)

"Hubble"s Survey of the Ultraviolet Universe: Panchromatic Extragalactic Research"" (SUPER)"
Windhorst, R. A., the "SUPER" Team 2013, BAAS, 221 (Abstract 228.03)

"Quasar Host Galaxies at z=2 and z=6: Point Source Subtraction With MCMC"
Mechtley, A., Koekemoer, A. M., Jahnke, J., Smith, B. M., Windhorst, R. A., Cohen, S. H., Fan, X., Hathi, N. P., Jansen, R., Jiang, L., Keel, W. C., Röttgering, H., Ryan, R. E., Scannapieco, E., Schneider, D. P., Schneider, G., Strauss, M. A., & Yan, H. 2013, BAAS, 221 (Abstract 339.31)

"Newborn Spheroidal Galaxies at High Redshift ($1 \lesssim z \lesssim 3$): When and How did the Old Stellar Populations that Dominate Today's Universe Form?"
Kaviraj, S., Cohen, S. H., Ellis, R. S., O'Connell, R. W., Windhorst, R. A., Silk, J., & the WFC3 Scientific Oversight Committee 2013, BAAS, 221, (Abstract 303.06)

"Mass Dependent Galaxy Transformation Mechanisms In The Complex Environment Of Super-Group Abell 1882"
Sengupta, A., Keel, W. C., Morrison, G. E., Windhorst, R. A., & Smith, B. 2013, BAAS, 221 (Abstract xxx.xx)

3f. OTHER JWST RELATED PUBLICATIONS, REPORTS, & PUBLIC OUTREACH:

For the record, all my JWST documents have been ITAR cleared, and all my JWST talks given in China use disposable memory sticks only — no laptops. All JWST work at ASU can be found at:
http://www.asu.edu/clas/hst/www/jwst/

Past JWST studies done at ASU can be found at:
http://www.asu.edu/clas/hst/www/jwst/jwststudies/

JWST related talks given by Rogier Windhorst can be found at:
http://www.asu.edu/clas/hst/www/jwst/jwsttalks/ and:
http://www.asu.edu/clas/hst/www/jwst/othertalks/

JWST related papers by Rogier Windhorst et al. can be found at:
http://www.asu.edu/clas/hst/www/jwst/papers/ and on:
http://xxx.lanl.gov/find/astro-ph and on:
http://adsabs.harvard.edu/abstract_service.html

The HUDF AHaH Java Tool developed for HST and JWST is available at:
http://www.asu.edu/clas/hst/www/jwst/HUDFjavatool/index.html
http://www.asu.edu/clas/hst/www/jwst/HUDFjavatool/download.html

Documentation of the AHaH code is available on:
http://www.asu.edu/clas/hst/www/jwst/HUDFjavatool/help.html

Related classroom exercises available for public outreach are available at:
http://www.asu.edu/clas/hst/www/jwst/HUDFjavatool/exercises.html or:
http://windhorst114.asu.edu/ or:
http://windhorst114.asu.edu/ahah/index.html

The HUDF clickable map, that is relevant for JWST, is available at:
http://www.public.asu.edu/~scohen/udf/ or:
http://www.asu.edu/clas/hst/www/jwst/clickonHUDF/index.html

4. COLLOQUIA/PUBLIC TALKS GIVEN BY ROGIER WINDHORST RELATED TO JWST:

In these talks either recent science results were discussed and their impacts on the design requirements of JWST, and/or a general review was given of the science goals of the JWST.

The main JWST talk that I further developed this year was on: "How can the James Webb Space Telescope measure "first light", Reionization, and Galaxy Assembly in the post Hubble WFC3 era?"

It was given in various forms (colloquium to scientists, seminar to undergraduate and graduate students, public talks to a general audience, museums, or amateur astronomy societies at various locations in Arizona.

The talk addresses (a subset of) the following issues:

- (1) What is JWST and how will it be deployed?
- (2) What instruments and sensitivity will JWST have?
- (3) How JWST can measure First Light and Reionization
- (4) How JWST can measure Galaxy Assembly
- (5) Predicted Galaxy Appearance for JWST at $z \simeq 1–15$
- (6) What can you do to speak up in support of JWST?

COLLOQUIA OR PUBLIC TALKS GIVEN BY ROGIER WINDHORST RELATED TO JWST

Date	Institute	Title
12/08/28	28^{th} IAU General Assembly (Beijing, China)	How JWST can measure First Light, Reionization, and Galaxy Assembly: Science & Project Update as of 2012
12/10/07	Exploring the Dark Universe: L. Z. Fang Workshop (UofA)	L.Z. Fang's astrophysics & China: Musings on First Light, Galaxy Assembly & Supermassive Blackhole Growth
13/01/08	221^{st} AAS Meeting; UV session (Long Beach, CA; invited review)	Hubble's Survey of the Ultraviolet Universe: Panchromatic Extragalactic Research ("SUPER")
13/03/18	ASU LOFAR Research Group (Tempe, AZ; invited seminar)	Observing AGN growth in radio, X-rays, with HST & JWST: When during galaxy assembly did AGN growth take place?
13/03/19	Spirit of the Senses (Tempe, AZ; invited public talk)	The best of Hubble, and what the James Webb Space Telescope will do after 2018
13/05/17	East Valley Astronomy Club (Gilbert, AZ; invited public talk)	The best of Hubble, and what the James Webb Space Telescope will do after 2018
13/05/19	U. of Nevada Graduation speech (Reno, NV; invited public talk)	Future careers at NASA: The best of Hubble, and what the James Webb Space Telescope will do after 2018
13/06/12	Kavli Workshop: Cosmology in the Era of ELT's (Chicago, IL)	Galaxy Assembly and AGN Growth with the Hubble WFC3 and with the James Webb Space Telescope
13/06/27	Australian National University (Canberra, ACT, Australia)	How will JWST measure First Light, Galaxy Assembly, & Supermassive Blackhole Growth: New Frontier after Hubble
13/07/01	Public Talk, Sydney Observatory (Sydney, NSW, Australia)	The best of Hubble, and what the James Webb Space Telescope will do after 2018
13/07/04	Macquarie University (Macquarie, NSW, Australia)	How will JWST measure First Light, Galaxy Assembly, & Supermassive Blackhole Growth: New Frontier after Hubble
13/07/12	Astronomical Soc. of Australia (Monash, VIC, Australia; review)	How will JWST measure First Light, Galaxy Assembly, & Supermassive Blackhole Growth: New Frontier after Hubble
13/07/18	CAASTRO First Light Workshop (Uluru, NT, Australia; invited)	Current and Future studies of First Light & Reionization: The James Webb Space Telescope and beyond
13/07/22	Swinburne Univ. of Technology (Hawthorne, VIC, Australia)	How will JWST measure First Light, Galaxy Assembly, & Supermassive Blackhole Growth: New Frontier after Hubble
13/07/23	The University of Melbourne (Melbourne, VIC, Australia)	How will JWST measure First Light, Galaxy Assembly, & Supermassive Blackhole Growth: New Frontier after Hubble
13/07/25	ICRAR/U. of Western Australia (Crawley, WA, Australia)	How will JWST measure First Light, Galaxy Assembly, & Supermassive Blackhole Growth: New Frontier after Hubble
13/07/26	ICRAR/Curtin University (Perth, WA, Australia)	How will JWST measure First Light, Galaxy Assembly, & Supermassive Blackhole Growth: New Frontier after Hubble

COLLOQUIA OR PUBLIC TALKS GIVEN BY ROGIER WINDHORST RELATED TO JWST

Date	Institute	Title
13/07/29	University of Sydney (Sydney, NSW, Australia)	How will JWST measure First Light, Galaxy Assembly, & Supermassive Blackhole Growth: New Frontier after Hubble
13/07/30	Australian Astronomical Observ. (North Ryde, NSW, Australia)	How will JWST measure First Light, Galaxy Assembly, & Supermassive Blackhole Growth: New Frontier after Hubble
13/07/31	Australian Telescope Nat'l Facility (Epping, NSW, Australia)	How will JWST measure First Light, Galaxy Assembly, & Supermassive Blackhole Growth: New Frontier after Hubble
13/09/07	Public Talk at Camp SESE Camp Tontozona (Payson, AZ)	The best of Hubble, and what the James Webb Space Telescope will do after 2018.
13/09/18	ASU Earth & Space Exploration SESE Colloquium (Tempe, AZ)	The best of Hubble's Wide Field Camera 3, & what the James Webb Space Telescope will do after 2018.
13/11/02	ASU Earth & Space Exploration Day (Public Talk; Tempe, AZ)	The best of Hubble, and what the James Webb Space Telescope will do after 2018.
13/11/09	SpaceVision 2013: Exploration & Development of Space (Tempe)	The best of Hubble, and what the James Webb Space Telescope will do after 2018.